

Lightcone mock catalogues from semi-analytic models of galaxy formation - I. Construction and application to the BzK colour selection

Alexander I. Merson^{1,2*}, Carlton M. Baugh¹, John C. Helly¹, Violeta Gonzalez-Perez¹, Shaun Cole¹, Richard Bielby¹, Peder Norberg¹, Carlos S. Frenk¹, Andrew J. Benson³, Richard G. Bower¹, Cedric G. Lacey¹, Claudia del P. Lagos¹

¹*Institute for Computational Cosmology, Department of Physics, University of Durham, South Road, Durham DH1 3LE, UK*

²*Department of Physics and Astronomy, University College London, Gower Street, London WC1E 6BT*

³*Carnegie Observatories, Pasadena, CA, U.S.A*

ABSTRACT

We introduce a method for constructing end-to-end mock galaxy catalogues using a semi-analytical model of galaxy formation, applied to the halo merger trees extracted from a cosmological N-body simulation. The mocks that we construct are *lightcone* catalogues, in which a galaxy is placed according to the epoch at which it first enters the past lightcone of the observer, and incorporate the evolution of galaxy properties with cosmic time. We determine the position between the snapshot outputs at which a galaxy enters the observer’s lightcone by interpolation. As an application, we consider the effectiveness of the BzK colour selection technique, which was designed to isolate galaxies in the redshift interval $1.4 < z < 2.5$. The mock catalogue is in reasonable agreement with the observed number counts of all BzK galaxies, as well as with the observed counts of the subsample of BzKs that are star-forming galaxies. We predict that over 75 per cent of the model galaxies with $K_{AB} \leq 23$, and $1.4 < z < 2.5$, are selected by the BzK technique. Interloper galaxies, outside the intended redshift range, are predicted to dominate bright samples of BzK galaxies (i.e. with $K_{AB} \leq 21$). Fainter K-band cuts are necessary to reduce the predicted interloper fraction. We also show that shallow B-band photometry can lead to confusion in classifying BzK galaxies as being star-forming or passively evolving. Overall, we conclude that the BzK colour selection technique is capable of providing a sample of galaxies that is representative of the $1.4 < z < 2.5$ galaxy population.

Key words: galaxy evolution; numerical techniques; semi-analytical modelling

1 INTRODUCTION

Modern galaxy surveys such as the Sloan Digital Sky Survey (SDSS, York et al. 2000) and the 2-degree Field Galaxy Redshift Survey (2dFGRS, Colless et al. 2001, 2003) have revolutionised our view of the galaxy distribution and have played a key role in shaping the constraints on our cosmological model (e.g. Norberg et al. 2001, 2002; Zehavi et al. 2005; Cole et al. 2005; Sánchez et al. 2006; Tegmark et al. 2006; Sánchez et al. 2009; Zehavi et al. 2011; Sanchez et al. 2012). The size of these surveys has heralded the start of an era of precision cosmology wherein we can measure statistics, such as the galaxy luminosity function, with random errors that are smaller than the systematic errors. To continue to make progress it is essential that we improve our understanding of how the estimation of such statistics is affected by the construction of a galaxy survey and the selection criteria applied. Mock galaxy

catalogues, which mimic the selection effects in real surveys, have emerged as an essential tool with which to achieve this aim, and play a central role in the analysis and exploitation of galaxy surveys.

When working with an observational galaxy catalogue, an estimator designed to recover a statistic, such as the luminosity function or correlation function, will have to compensate for a variety of effects such as non-uniform coverage of the sky and a selection function that varies strongly with radial distance from the observer. The primary advantage of a mock catalogue is that, by construction, we already know the ‘true’ answer for the statistic without these effects. By comparing a measurement extracted from a synthetic mock catalogue with the ideal result (i.e. the statistic measured using a complete sample of galaxies from the original simulation cube), one can adjust and tune the performance of the estimator to reduce any systematic effects. A prime example is that of algorithms designed to find groups of galaxies, the calibration of which requires foreknowledge of the underlying dark matter halo

* E-mail: a.i.merson@durham.ac.uk

distribution in order to test how faithfully the algorithm can recover these structures when working in redshift space (Eke et al. 2004; Robotham et al. 2011; Murphy et al. 2012). Additionally, mock catalogues can be used to forecast the scientific return of future galaxy surveys (Cole et al. 1998; Cai et al. 2009; Orsi et al. 2010). Therefore they can help shape the design of a survey by assessing the level, and quality, of the statistics recoverable with any particular configuration. Finally, mock catalogues allow us to cast the predictions of theoretical models of galaxy formation in a form that can be directly compared against observables.

In this paper we present a method for building mock catalogues for galaxy surveys, which can cover any redshift range. Mock catalogues constructed in this way have already been used extensively by the Galaxy And Mass Assembly (GAMA) survey (Driver et al. 2009, see also Robotham et al. 2011; Alpaslan et al. 2012). Here, we illustrate the power of mock catalogues by evaluating the performance of the BzK colour selection technique, which was designed to isolate galaxies in the redshift interval $1.4 < z < 2.5$ (Daddi et al. 2004a). This redshift range is an exciting one for galaxy assembly, since it is thought that most of the stellar mass of many of the progenitors of present day massive galaxies formed during this period (Madau et al. 1998; Dickinson et al. 2003). Unfortunately this epoch lies within the ‘redshift desert’ where the spectroscopic measurement of galaxy redshifts is difficult due to the lack of strong spectral features at optical wavelengths. Only recently, with the development of near-infrared (NIR) spectroscopy, have large galaxy surveys begun to probe this region and to assess the build-up of galaxies over this crucial period (e.g. Franx et al. 2003; van Dokkum et al. 2003).

Prior to this, knowledge of the galaxy population in the ‘desert’ was derived from photometry. This led to the development of colour selection techniques designed to efficiently identify targets for spectroscopic follow-up (which is much more expensive). A well-known example of this is the Lyman-break dropout technique, proposed by Steidel et al. (1996, 2003, 2004), which identifies star-forming galaxies at $z \sim 3 - 10$ according to their rest-frame ultraviolet colours and sampling of the Lyman break spectral feature. Other examples include extremely red objects at $z \sim 1$ (Elston et al. 1988; McCarthy 2004) and distant red galaxies at $z \sim 2$ (Franx et al. 2003).

A popular photometric technique, designed to simultaneously identify populations of star-forming and passively evolving galaxies, is the BzK colour-criterion (Daddi et al. 2004a). This approach, which selects galaxies based on their $(B - z)$ and $(z - K)$ colours, is designed to deliver galaxy samples within the redshift range $1.4 < z < 2.5$ that are not biased by the presence of dust or by the age of their stellar populations (Kong et al. 2006; Hayashi et al. 2007, 2009; Grazian et al. 2007; Hartley et al. 2008; Lin et al. 2011).

Early studies of $K_{AB} \lesssim 22^1$ BzK-selected galaxies revealed them to typically have large stellar masses, $\sim 10^{11} h^{-1} M_{\odot}$, and, in the case of those labelled as star-forming, high star-formation rates, $\sim 100 h^{-1} M_{\odot} \text{yr}^{-1}$ (Daddi et al. 2004a,b, 2005a,b; Reddy et al. 2005; Kong et al. 2006). Such properties, combined with high metallicities (e.g. Daddi et al. 2004a; Hayashi et al. 2009) and indications that these systems are strongly clustered (Hayashi et al. 2007; Hartley et al. 2008; Blanc et al. 2008), have led many au-

thors to speculate that BzK galaxies are the high-redshift precursors of massive early-type galaxies found in groups and clusters at the present day. The key question we address here is: Are the properties of the bright galaxies identified by this selection technique representative of the overall population with $1.4 < z < 2.5$, or are we really just seeing a special subclass of galaxies? If the latter is true, is this simply because current observations have not been sufficiently deep to see the fainter, more representative galaxies or is the BzK criterion somehow biased towards selecting a subset of the galaxy population? A galaxy mock catalogue is a vital resource in helping to answer these questions by allowing an assessment of the effects of observational selection on the completeness of the galaxy sample as well as an examination of whether or not the BzK criterion is sensitive to the intrinsic properties of galaxies.

The layout of the paper is as follows: In section 2 we summarise the various methods used to construct mock galaxy catalogues. In section 3, we introduce the numerical simulation and galaxy formation model that we will use as inputs, before, in section 4, providing further details of our method for constructing lightcone mock catalogues. This section provides a full overview of the lightcone construction, including the assignment of positions to model galaxies. In section 5 we use a lightcone mock catalogue to assess the performance of the BzK selection technique. Note that this application only uses some features of the lightcone; the clustering of BzK galaxies will be dealt with in a separate paper. Finally, in section 6, we summarise our method and present our conclusions. Throughout this paper we use magnitudes in the AB system.

2 CONSTRUCTING MOCK CATALOGUES

In this section we provide an overview of the basic procedure for constructing mock catalogues and set out the advantages of using a semi-analytical model of galaxy formation.

2.1 Overview of the technique

A very basic mock catalogue could be constructed by randomly sampling one of the measured statistical distributions that describe the galaxy population (e.g. the luminosity function or stellar mass function). Although the resulting catalogue of galaxies would match that particular statistic (by construction), without any further information about the galaxies, such as their colour or spatial distribution, the mock would be very limited.

Building a more realistic mock catalogue, with positional information and including other galaxy properties and their evolution, requires the use of a numerical simulation which follows the growth of structure in the dark matter. The procedure for constructing mock catalogues from a numerical simulation can be broken down into the following steps: (i) generate a population of galaxies either empirically or using a physical model, using either the dark matter distribution or dark matter halos, (ii) place these galaxies into a cosmological volume, (iii) apply the angular and radial selection functions of the survey.

2.1.1 Generating a galaxy population

To generate a population of galaxies one must first model the distribution of dark matter, which is often done with a N-body simulation. Dark matter only N-body simulations allow us to build halo

¹ Daddi et al. (2004a) originally used a $K_{Vega} \leq 20$ selected sample. We have converted this to the AB system using the K-band conversion from Blanton & Roweis (2007), where $m_{AB} - m_{Vega} = 1.85$.

populations using gravity alone. The full spatial information provided by N-body simulations allows one to extract clustering information, which would otherwise not be available if a Monte-Carlo approach was to be used. Additionally, the merger histories of halos in N-body simulations will also include environmental effects, such as halo assembly bias (Gao et al. 2005).

The way in which dark matter halos are populated with galaxies is where the methods of mock catalogue construction can differ. Blaizot et al. (2005) (see also Baugh 2008) summarise several of the different methods available, which include using phenomenological models to assign galaxies to dark matter particles in the simulation (e.g. Cole et al. 1998) or using empirically derived statistics, such as the *halo occupation distribution* (HOD, Berlind & Weinberg 2002; Song et al. 2012) or *sub-halo abundance matching* (Vale & Ostriker 2004). Other, more physical approaches are also possible. For instance, one could include the baryons in the original simulation, using either a grid-based or particle-based method to solve the hydrodynamical equations. The problem with direct, hydrodynamical simulations however, is that they are computationally expensive and so, in practice, are restricted to small volumes (e.g. the $25h^{-1}\text{Mpc}$ and $100h^{-1}\text{Mpc}$ boxes used in the Overwhelmingly Large Simulations project of Schaye et al. 2010).

A powerful approach, that we choose to adopt, is to use a *semi-analytical model* of galaxy formation to populate the halo merger trees extracted from a high resolution, cosmological N-body simulation (Diaferio et al. 1999; Benson et al. 2000; Blaizot et al. 2005; Kitzbichler & White 2007; Sousbie et al. 2008; Overzier et al. 2009; Cai et al. 2009; Henriques et al. 2012; Overzier et al. 2012). Modelling of various physical processes, such as the cooling of gas within dark matter halos, is necessary to follow the baryonic component and predict the fundamental properties of galaxies, such as their stellar mass and star formation history. The adoption of an *initial mass function* (IMF), a *stellar population synthesis* (SPS) model and a treatment of dust extinction allows these fundamental properties to be connected with observables, thus enabling a direct comparison between observations and the predictions of the galaxy formation model.

2.1.2 Generating a cosmological volume

Current and future galaxy surveys are designed to probe ever larger cosmological volumes. As a result there is a growing demand for simulations with boxes of sufficient size to match the volumes of these surveys. Unfortunately, current computing power means that a compromise must often be made between the volume of the simulation box and the resolution at which the simulation is carried out. Therefore a sufficiently large cosmological volume can only be sampled by tiled replication of a smaller box simulation. For very shallow galaxy surveys (e.g. with a median redshift $z \lesssim 0.05$), the lookback time is sufficiently small that typical galaxy properties will not have undergone significant evolution across the redshift interval covered by the survey. In these instances, the statistics of the galaxy population at the extremes of the survey will not be too dissimilar to the statistics today and so one can build a mock catalogue using galaxies from a single simulation snapshot. However, for very deep galaxy surveys which cover a significant lookback time, we would expect to see substantial evolution in galaxy properties and in the growth of large-scale structure. Therefore more sophisticated mock catalogues, that tile the survey volume using many different simulation snapshots, are required to adequately reproduce the evolution seen in the properties of galaxies and their clustering. The mock catalogues that we construct in this work are

lightcone mock catalogues, in which galaxies are placed according to the epoch at which they first cross the observer’s past lightcone, i.e. at the location at which the light emitted from the galaxy has just enough time to reach the observer, and thus incorporate the evolution of structure with cosmic time.

Finally, observations will be subject to uncertainties or biases, introduced as a result of survey design or selection effects, and so to properly relate theoretical predictions to observations we must subject the simulated data to the same selection functions as the observed galaxy sample.

2.2 Why use a semi-analytical galaxy formation model?

Modelling the formation of galaxies is a difficult task. Part of the problem is that our knowledge of the underlying physics is limited and so we cannot simply write down a precise formulation for every process. Furthermore, despite the continued development of direct, hydrodynamic simulations, current computational capabilities mean that many of the relevant processes (for example star formation or supernova feedback) remain firmly below the resolution limits of direct simulations and can only be addressed through “sub-grid” physics. Semi-analytic models describe the sub-grid physics using physically motivated, parametrised equations that follow the evolution of baryons trapped in the gravitational potential wells of hierarchically grown dark matter halos (White & Rees 1978; Cole 1991; White & Frenk 1991; Kauffmann et al. 1993; Cole et al. 1994; for reviews of the semi-analytical approach see Baugh 2006 and Benson 2010). There are several compelling advantages to using semi-analytic models for building mock catalogues:

(i) The development of deep, wide-field photometric galaxy surveys spanning large cosmological volumes has led to demand for large (suites of) mock catalogues that can be constructed rapidly and accurately. Semi-analytic modelling is currently the only physical approach that meets these ideals: such models are capable of populating large cosmological volumes with galaxies much faster and at a lower computational cost than is currently possible with hydrodynamical simulations.

(ii) The modular design of semi-analytic models allows new physics to be incorporated readily. Combined with their short runtime, this means that semi-analytic models can be tuned to match observations quickly, in response to a change to the background cosmology or to the galaxy formation physics. Moreover, the larger computational box that can be used in the N-body and semi-analytical approach, compared with a hydrodynamical simulation, means that the clustering predictions are robust out to larger scales.

(iii) Empirically motivated methods, such as HOD modelling, must first be calibrated against observational data, (e.g. the Las-Damas mock catalogues, McBride et al. 2009). Hence, mock catalogues built using such methods are limited by the availability of observational data at high redshift. Furthermore, the data that is available may be affected by sample variance leading to unrepresentative HOD parameters being fitted. Semi-analytic models however, once tuned to fit the observations of galaxies at low redshift, can *predict* galaxy properties out to high redshift, without further observational input. Mock catalogues built from semi-analytical models are therefore much more flexible than catalogues constructed using other methods.

(iv) The next generation of galaxy surveys will map the sky across a large portion of the electromagnetic spectrum, with multi-wavelength follow-up observations resulting in potentially complex survey selection functions, such as for the Galaxy And Mass As-

sembly (GAMA) Survey (Driver et al. 2011). Ideally mock catalogues for future surveys need to provide a diverse range of galaxy properties as well as providing the capability to select galaxies simultaneously in multiple bands. Semi-analytic models model the complete star formation history for each galaxy and so can predict many different galaxy properties. Mock catalogues based upon semi-analytic models are already capable of mimicking sophisticated multi-band selection criteria.

3 GALAXY FORMATION MODEL

The model we adopt to generate the galaxy population for our mock catalogues is the Bower et al. (2006) variant of the GALFORM semi-analytic model (Cole et al. 2000). To build realistic lightcone mock catalogues we require spatial information, so we use dark matter halo merger trees extracted from the *Millennium Simulation* (Springel et al. 2005).

3.1 The Millennium Simulation

3.1.1 Cosmology and parameters

The population of dark matter halos for our mock catalogues is provided by the *Millennium Simulation*, a 2160^3 particle N-body simulation of the Λ CDM cosmology carried out by the Virgo Consortium (Springel et al. 2005). This simulation follows the hierarchical growth of cold dark matter structures from redshift $z = 127$ through to the present day in a cubic volume of size $500h^{-1}\text{Mpc}$ on a side. Halo merger trees are constructed using particle and halo data stored at 64 fixed epoch snapshots that are spaced approximately logarithmically in expansion factor. The Millennium trees have a temporal resolution of approximately 0.26 Gyr at the present day, with approximate resolutions of 0.38, 0.35, 0.26 Gyr at redshifts $z = 0.5, 1, 2$ respectively. Halos in the simulation are resolved with a minimum of 20 particles, corresponding to a halo resolution of $M_{\text{halo,lim}} = 1.72 \times 10^{10} h^{-1} M_{\odot}$, significantly smaller than expected for the Milky Way’s dark matter halo.

The cosmological parameters adopted in the *Millennium Simulation* are: a baryon matter density $\Omega_b = 0.045$, a total matter density $\Omega_m = \Omega_b + \Omega_{\text{CDM}} = 0.25$, a dark energy density $\Omega_{\Lambda} = 0.75$, a Hubble constant $H_0 = 100h \text{ km s}^{-1} \text{ Mpc}^{-1}$ where $h = 0.73$, a primordial scalar spectral index $n_s = 1$ and a fluctuation amplitude $\sigma_8 = 0.9$. These parameters were chosen to match the cosmological parameters estimated from the first year results from the Wilkinson Microwave Anisotropy Probe (Spergel et al. 2003).

3.1.2 Construction of halo merger trees

To construct the halo merger trees one must first identify groups of dark matter particles in each of the simulation snapshots. This is done using the *Friends-Of-Friends* algorithm (FOF, Davis et al. 1985). The *Millennium Simulation* was carried out with a specially modified version of the GADGET2 code (Springel 2005) with a built-in FOF group-finder, allowing FOF groups to be identified on the fly. The algorithm SUBFIND (Springel et al. 2001) was then used to identify self-bound, locally over-dense sub-groups within the FOF groups. This procedure typically results in the bulk of the mass of a FOF group being assigned to one large sub-group which represents the background mass distribution of the halo. The remaining mass is usually split between smaller satellite sub-groups

orbiting within the halo and unbound “fuzz” particles which are not associated with any sub-group.

However, it is not uncommon for the FOF algorithm to join together structures which might be better considered to be separate halos for the purposes of semi-analytic galaxy formation. For example, nearby groups may be linked by tenuous “bridges” of particles or they may only temporarily be joined. The merger tree algorithm we use in this work is intended to deal with these cases and ensure that the resulting trees are strictly hierarchical, i.e. once two halos are deemed to have merged they should remain merged at all later times.

The first step in the construction of the merger trees is to identify a descendant for each sub-group at the next snapshot. The descendant of each sub-group is identified as the sub-group at the next snapshot that contains the largest number of the N_{link} most bound particles, where

$$N_{\text{link}} = \max(f_{\text{trace}} N_p, N_{\text{linkmin}}), \quad (1)$$

with $N_p \geq 20$, as already stated, and f_{trace} and N_{linkmin} are set to 0.1 and 10 respectively. Defining N_{link} in this way means that in well resolved cases we follow the most bound “core” of the sub-group, which is important for satellite sub-groups which may be tidally stripped of their outer parts. For the smallest groups with $N_p \sim 20$, $N_{\text{link}} = 10$ so we are following up to 50% of the particles and so preventing inaccurate assignment due to low number statistics.

The SUBFIND algorithm occasionally temporarily “loses” a sub-group between snapshots. For example, a sub-group may be identified at snapshot i , lost at one or more subsequent snapshots, and then identified again at snapshot $i + n$, where $n > 1$. This can happen if a small, isolated group briefly falls below the resolution limit or if a satellite sub-group passes close to the centre of its host halo. In either case we would like to identify the sub-group at snapshot $i + n$ as the descendant of the sub-group at snapshot i . Our approach to achieve this aim is as follows:

- (i) Identify sub-groups which may have been lost by SUBFIND.
- (ii) Identify sub-groups which may have just been reacquired by SUBFIND.
- (iii) Attempt to locate descendants of the sub-groups in (i) with the sub-groups in (ii).

Groups which are “lost” are identified by looking for groups which either have no immediate descendant or are not the most massive progenitor of their immediate descendant. Some of these groups will have been lost because they have genuinely been disrupted and absorbed into the parent halo, but some will reappear later. Groups which have just been reacquired are identified by looking for “orphan” sub-groups, i.e. groups with no immediate progenitors.

For each lost sub-group at snapshot i (where i is not the present day), we examine the orphan sub-groups at snapshot $i + 2$, $i + 3$, ..., $i + N_{\text{step}}$. An orphan sub-group is identified as the descendant of a lost sub-group if at least a fraction f_{link} of the N_{link} most bound particles from the lost group are in the orphan group and no orphan descendant can be found at earlier snapshots. We usually set $N_{\text{step}} = 5$ and $f_{\text{link}} = 0.5$.

If this procedure results in the identification of a descendant for a sub-group, then that descendant will be used in the subsequent stages of the construction of the merger trees. For all other sub-groups the descendant is taken to be the immediate descendant at the next snapshot. For the construction of merger trees, having a sub-group and its descendant separated by multiple snapshot out-

puts is not a problem. However, this is inconvenient for codes, such as GALFORM, which expect the descendant of a subhalo to always be found in the next snapshot. To avoid this, for those subhalos that are temporarily lost, interpolated sub-halos are inserted at each snapshot where the sub-halo is ‘missing’. For very high resolution simulations this is a common occurrence. However, for simulations like the *Millennium Simulation* such interpolated sub-halos are rare.

Next, the sub-groups at each snapshot are organised into a hierarchy of halos, sub-halos, sub-sub-halos etc.. For each sub-group in a FOF group we identify the least massive of any more massive “enclosing” sub-groups in the same FOF group. Sub-group A is said to enclose sub-group B if B’s centre lies within twice the half mass radius of A. Any sub-group which is not enclosed by another is considered to be an independent halo. We also consider a sub-group to be an independent halo if it has retained at least 75 per cent of the maximum mass it has ever had while being the most massive sub-group in its FOF group. This is because we expect a halo involved in a genuine merger with a more massive halo to be stripped of mass. In either case, if a sub-group is deemed to be an independent halo then any sub-groups it encloses are also assigned to that halo.

At this stage we have, for each snapshot, a population of halos, each of which consists of a grouping of `SUBFIND` sub-groups with pointers linking each sub-group with its descendant at the next snapshot. We choose the descendant of a halo to be the halo at the next snapshot which contains the descendant of the most massive sub-group in the halo. This defines the halo merger tree structure.

The GALFORM model assumes that when a halo merges with another, more massive “host” halo, that its hot gas is stripped away so that no further gas can cool in the less massive halo. Since a halo can only be stripped of hot gas once, we wish to treat these objects as satellite sub-halos within their host halo for as long as they survive in the simulation, even if their orbit puts them outside the virial radius of their host halo at some later times. We therefore attempt to identify cases where halos fragment, and re-merge them.

In practice we implement this by looking for satellite sub-groups which split off their host to become independent halos at the next snapshot. A sub-group will be re-merged if it satisfies all of the following conditions:

- The sub-group is the most massive progenitor of its descendant. This is taken to mean that the sub-group survives at the next snapshot.
- The sub-group is not the most massive sub-group in its halo. This indicates that it is a satellite sub-halo within a larger halo.
- The descendant of the sub-group is the most massive group in its halo.
- The descendant of the sub-group belongs to a halo other than the descendant of the halo containing the original sub-group. This indicates that the host halo has fragmented.

The last condition is necessary because a sub-group can sometimes become the most massive in its parent halo without any halo fragmentation occurring, especially if the halo consists of two sub-groups of similar mass. If these conditions are met, the halo containing the descendant of the satellite sub-group is merged with the descendant of the host halo.

Following this post-processing, we are left with, for the *Millennium Simulation*, approximately 20 million halo merger trees with, in total, approximately 1 billion nodes.

3.2 The GALFORM semi-analytic model

The Durham semi-analytical galaxy formation model, GALFORM, originally developed by Cole et al. (2000), models the star formation and merger history of a galaxy and makes predictions for many galaxy properties including luminosities over a substantial wavelength range extending from the far-UV through to the sub-millimetre (Baugh et al. 2005; Lacey et al. 2008, 2010; Lagos et al. 2011a; Fanidakis et al. 2011; Lagos et al. 2012).

3.2.1 Model overview

The GALFORM model populates a distribution of dark matter halos with galaxies by using a set of coupled differential equations to determine how, over a given time-step, the “subgrid” physics regulate the size of the various baryonic components of galaxies. GALFORM models the main physical processes governing the formation and evolution of galaxies: (i) the collapse and merging of dark matter (DM) halos, (ii) the shock-heating and radiative cooling of gas inside DM halos, leading to the formation of galactic disks (iii) quiescent star formation in galactic disks, (iv) feedback as a result of supernovae, active galactic nuclei and photo-ionisation of the inter-galactic medium, (v) chemical enrichment of stars and gas and (vi) dynamical friction driven mergers of galaxies within DM halos, capable of forming spheroids and triggering starburst events. The prescriptions describing these physical processes are described in a series of papers: Cole et al. (2000); Benson et al. (2003); Baugh et al. (2005); Bower et al. (2006); Font et al. (2008); Lacey et al. (2008); Lagos et al. (2011b), as well as in the reviews by Baugh (2006) and Benson & Bower (2010).

The star-formation history of a galaxy can be determined by tracking the star-formation rate, SFR, and chemical enrichment predicted in its progenitors. Convolving this with a model SSP (single stellar population) allows one to predict the spectral energy distribution (SED) of the galaxy, which in turn can be sampled by filter transmission curves to predict rest-frame magnitudes in various ultraviolet (UV), optical, near-infrared and far-infrared bands. Given the redshift of a galaxy, the fixed filter transmission curves can be shifted by an appropriate amount to obtain observer-frame magnitudes. Dust extinction is incorporated by assuming the dust (whose mass is predicted by the chemical evolution model) is mixed together with the stars in the disk of the galaxy in two phases: in clouds and in a diffuse component (see Granato et al. 2000). Assuming a distribution of dust grain sizes, and combining this with the predicted scalelengths of the disk and bulge, allows one to calculate the optical depth and apply the appropriate attenuation to the luminosity at various wavelengths. We use the stellar population synthesis model of Bruzual & Charlot (a version from 1999, that is described in Bruzual & Charlot 2003) and assume a Kennicutt (1983) IMF in all modes of star formation.

We set the adjustable parameters in GALFORM by requiring that the model predictions match a subset of observations, primarily of the local galaxy population. We have traditionally assigned more weight in this process to matching the optical and near-infrared luminosity functions (see e.g. Bower et al. 2010, for a discussion of an automated version of this process). The requirement of matching the observed luminosity function has led to the inclusion of different feedback mechanisms to regulate star formation. Feedback from stellar winds and supernovae (SNe) is important for reheating cold gas (and thus quenching the star formation) in small halos. This process has been shown to allow the models to reproduce the faint end of the observed galaxy luminosity function (Benson

et al. 2003). The major extension made in Bower et al. (2006) was the introduction of feedback due to active-galactic nuclei (AGN), which quenches the cooling flow in massive, quasi-static hot halos and consequently shuts down star formation in their central galaxies. This proposed solution to the *over-cooling problem* that had long plagued models of galaxy formation (e.g. Benson et al. 2003), proved necessary to explain the break in the luminosity function, allowing the model to reproduce the b_J -band and K-band luminosity functions (including the evolution at the bright end) out to redshift $z \sim 2$. In addition, the Bower et al. model is able to accurately predict the evolution of the galaxy stellar mass function out to $z \sim 5$ (Bielby et al. 2011), successfully reproduce the clustering and abundance of luminous red galaxies as seen in the SDSS (Almeida et al. 2008), produce a bimodal distribution of galaxy colours that is in good agreement with observations of the SDSS (González et al. 2009) and match the number counts and redshift distribution of extremely red objects (Gonzalez-Perez et al. 2009).

The GALFORM calculation uses dark matter merger histories extracted from the Millennium simulation. As commented upon above, this simulation has 64 snapshots. Information about the baryonic content of galaxies is tracked on finer timesteps, with 8 “sub-steps” inserted between the N-body output times. Parts of the calculation, for example the luminosity of the composite stellar population can be followed on an even finer time grid, determined by an adaptive differential equation solver.

3.2.2 Placement of galaxies in halos

In the GALFORM model, the treatment of the properties of a galaxy will depend upon its status within its host halo, i.e. whether it is a central or a satellite galaxy. Central galaxies are placed at the centre of the most massive sub-halo of the host halo and are the focus for all gas that is undergoing cooling. In the event of a halo merger, we choose the central galaxy of the main (most massive) progenitor halo as the central galaxy of the descendant halo, with any other galaxies becoming satellites. It should be noted that according to this definition, the central galaxy of each (sub)halo need not be the most luminous or the one with the largest stellar mass.

Following a halo merger, the central galaxy of the less massive progenitor halo becomes a satellite galaxy of the descendant halo. If the most massive sub-halo of the less massive progenitor can no longer be resolved (i.e. the sub-halo now has fewer than 20 particles and has been lost), then the galaxy is placed on what was the most bound particle in that sub-halo. Satellite galaxies are stripped of their hot gas, thus quenching any further cooling and inhibiting long-term star-formation (see Font et al. 2008, for an alternative cooling model for satellites).

A merger timescale is calculated based upon the initial energy and angular momentum of the satellite’s orbit (which is chosen at random), as well as the mass of the satellite and the mass of the halo hosting the central galaxy and satellite system. It is expected that after this time the effects of dynamical friction will have caused the satellite to merge with the central galaxy. However, the merger timescale of a satellite is recalculated every time the satellite’s host halo merges and becomes a sub-halo of a more massive halo (see Cole et al. 2000).

4 LIGHTCONE CONSTRUCTION

We now outline the method adopted to construct lightcone mock catalogues. Our scheme shares many features in common with the

methods used by Blaizot et al. (2005) and Kitzbichler & White (2007), with some improvements.

By first running the GALFORM model² on the halo merger trees of the *Millennium Simulation* we generate a galaxy population that is used to build the lightcone catalogues. Galaxy properties are stored for each fixed, snapshot epoch that falls within the redshift range of interest for a particular survey.

An observer is then placed inside the simulation box at a position that can be set manually³ or at random.

4.1 Replication of the simulation box

The cosmology used in the Millennium Simulation means that the simulation box side-length, $L_{\text{box}} = 500h^{-1}\text{Mpc}$, corresponds to the co-moving distance out to $z = 0.17$. Therefore, in order to generate a cosmological volume that is of sufficient size to fully contain any galaxy survey that extends out to a modest redshift, it is necessary to tile replications of the simulation box (see the discussion in § 2.1.2).

The number of replications per axis, n_{rep} , that need to be stacked around the original box (containing the observer) is given by,⁴

$$n_{\text{rep}} = \left\lceil \frac{r_{\text{max}}}{L_{\text{box}}} \right\rceil + 1, \quad (2)$$

where r_{max} is the maximum co-moving radial distance that we want to reach in the final mock catalogue. Including the original simulation box, we have a total of $(2n_{\text{rep}} + 1)^3$ replications. The Cartesian co-ordinate system, $(\hat{\mathbf{X}}, \hat{\mathbf{Y}}, \hat{\mathbf{Z}})$, of the combined ‘super-cube’ is then translated so that the observer is located at the origin.

An unfortunate consequence of generating a large volume in this way is that structures can appear repeated within the final lightcone volume. Although repeated structures cannot have a co-moving separation less than the simulation box side-length, if any repeated structures have small angular separations when projected onto the ‘mock sky’, then projection-effect artefacts can be introduced into the catalogue. Blaizot et al. (2005) illustrate the effect of these artefacts, along with possible methods for eliminating them. One method that they demonstrate to be effective is to apply random sequences of $\pi/2$ rotations and reflections to the replicated boxes so that any repeated structures are viewed at different orientations and appear as different structures. The problem with this approach is that, due to the periodic boundary conditions of the N-body simulation, when tiling the replications, any transformation besides a translation would add undesirable discontinuities into the underlying density field. However, if for example one wishes to extract clustering statistics, the underlying density field should be preserved. We therefore choose not to use this method in the construction of our lightcone catalogues.

4.2 Orientating the observer

Our aim when orientating the observer is to be able to define a right-handed Cartesian co-ordinate system, $(\hat{\mathbf{X}}', \hat{\mathbf{Y}}', \hat{\mathbf{Z}}')$, such that the

² We stress that our lightcone construction algorithms are independent of choice of semi-analytic model and can be run using any input galaxy formation model.

³ Often one will choose to position the observer manually if they desire the observer to be placed in a specific location, such as an environment similar to the Local Group.

⁴ $\lceil x \rceil$ means that x is rounded down to the nearest integer.

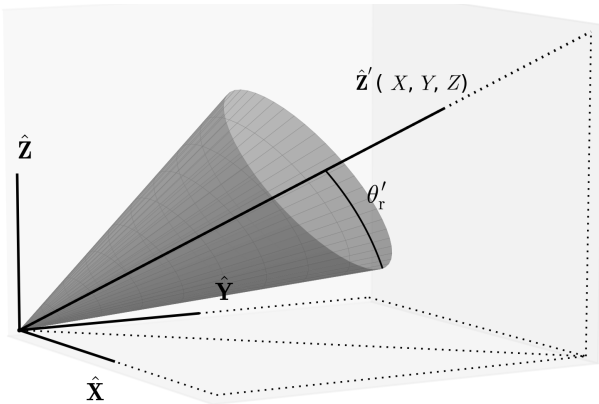


Figure 1. Schematic of lightcone geometry. The axis $\hat{\mathbf{Z}}'$ defines the central *line-of-sight* vector of the observer. The angle θ'_r defines the angular size of the field-of-view of the lightcone. Any galaxy whose position vector, $\vec{r}'(X', Y', Z')$, is offset from the $\hat{\mathbf{Z}}'$ axis by an angle $\theta' > \theta'_r$ is excluded from the lightcone.

observer is looking down the $\hat{\mathbf{Z}}'$ axis, as illustrated in Fig. 1. This axis defines the central axis of symmetry of the conical volume of the lightcone and points to the centre of the field of the lightcone on the mock sky, i.e. $\hat{\mathbf{Z}}'$ points along the central *line-of-sight* vector of the observer. The half-opening angle, θ'_r , governs the angular extent of the field-of-view of the lightcone (see §4.3). The orientation of the observer is simply how we describe this vector, $\hat{\mathbf{Z}}'$, in terms of the global Cartesian axes of the “super cube”, $\hat{\mathbf{Z}}'(X, Y, Z)$.

For deep, pencil-beam mock catalogues, carefully choosing the orientation of the observer can minimise, or even remove, structure repetition. The approach adopted by Kitzbichler & White (2007) is to orientate the observer in a ‘slanted’ direction, with respect to the Cartesian axes of the simulation box, so that the observer is not looking along any of the Cartesian axes or the cube diagonals (along which structure repetition can introduce noticeable artefacts). By defining the central line-of-sight of the observer as $\hat{\mathbf{Z}}'(X, Y, Z) = (n, m, nm)$, where m and n are integers with no common factor, Kitzbichler & White are able to construct lightcone catalogues with a near-rectangular sky coverage of $1/m^2 n \times 1/n^2 m$ (radians) in which the first repeated structure will lie at distance of $\sim mnL_{\text{box}}$ from the observer.⁵ When constructing lightcone catalogues for which we wish to minimise duplicated structures, albeit at the expense of the solid angle of the catalogue, we adopt this approach. This is necessary for applications considering, for example, the angular clustering of galaxies, where projection effects could severely distort the clustering signal.

Once we are satisfied with the chosen orientation of $\hat{\mathbf{Z}}'$, we define the axis $\hat{\mathbf{X}}'$ (to be perpendicular to both $\hat{\mathbf{Z}}'$ and $\hat{\mathbf{X}}$) and the axis $\hat{\mathbf{Y}}'$ (to be perpendicular to both $\hat{\mathbf{X}}'$ and $\hat{\mathbf{Z}}'$).

4.3 Finalising the lightcone geometry

Now that we know the location and orientation of the observer we can set about applying the necessary geometrical cuts to construct

the lightcone volume. The first step is to isolate a spherical volume about the observer, with a co-moving radius, r_{max} , whose value is sufficiently large that, given the flux limits of the survey we wish to emulate, we would expect to be well into the high-redshift tail of the galaxy redshift distribution (such that only a negligible fraction of the brightest, high redshift galaxies are missed). This radial cut is applied to help speed up the calculation so that we are not searching for galaxies in box replications that are too far from the observer to contribute a significant number of objects to the mock catalogue. For boxes with a fraction of their volume lying within r_{max} , we check when each galaxy will enter the observer’s past lightcone (see §4.4). If a galaxy enters the lightcone at a distance greater than r_{max} (or it never enters the lightcone at all) then it is discarded.

Next we apply an angular cut on the mock galaxies, which is dictated by the solid angle of the galaxy survey we wish to mimic. The solid angle in steradians, Ω , of the mock catalogue is defined by

$$\Omega = 2\pi [1 - \cos(\theta'_r)], \quad (3)$$

where θ'_r is the field-of-view angle of the catalogue. By varying the value of θ'_r , we can construct lightcones with solid angles ranging from pencil beams, to all-sky (2π) surveys.⁶ Following this cut, the catalogue volume resembles the sector of a sphere, with half-opening angle θ'_r and $\hat{\mathbf{Z}}'$ as its axis of symmetry. For those boxes whose volume overlaps that of the catalogue, we calculate the position at which each galaxy enters the lightcone. Using this position we calculate the angle θ' , the angle between the position vector of the galaxy and the $\hat{\mathbf{Z}}'$ axis, and discard any galaxy with $\theta' > \theta'_r$, that lies outside the solid angle of the catalogue.

Finally, for those galaxies that are successfully included in the lightcone, we determine their right-ascension, α , and declination, δ , on the mock ‘sky’. We do this by first defining a sky coordinate system such that the observer’s central line-of-sight vector, $\hat{\mathbf{Z}}'$, points towards a right ascension, α_0 , and declination, δ_0 , on the sky. We then determine the sky position of a galaxy by passing $\vec{r}(X, Y, Z)$, through the transformation, $\mathcal{R}_Z(\alpha_0)\mathcal{R}_Y(\pi/2 - \delta_0)\vec{r}$, where \mathcal{R}_Z and \mathcal{R}_Y are the standard 3-dimensional Cartesian rotation matrices about the $\hat{\mathbf{Z}}$ and $\hat{\mathbf{Y}}$ -axes respectively. (We assume that lines of constant declination lie parallel to the $X - Y$ plane, so do not apply any rotation about the X axis).

4.4 Positioning galaxies within the lightcone

The lightcone selection of galaxies is carried out by identifying those galaxies whose light has sufficient time to reach the observer. However, before one can calculate when a galaxy enters the lightcone, one must determine the epoch at which its host dark matter halo enters the observer’s past lightcone.

4.4.1 Placement of halo centres

A halo, located at $\vec{r}(X, Y, Z, t)$, at a lookback time, t , will be “visible” to the observer at all instances where $|\vec{r}(X, Y, Z, t)| \leq r_c(t)$,

⁵ Carlson & White (2010) adopt a similar approach to Kitzbichler & White by performing volume remapping of the original simulation box such that the mock catalogue geometry can fit inside the new geometry without the need for box replication.

⁶ By setting $\theta'_r = \pi$ we can construct all-sky lightcone catalogues. When constructing such catalogues we can apply an additional geometrical cut to remove galaxies that would be obscured by the plane of the Milky Way. Having calculated the celestial co-ordinates of the galaxy on the mock sky, we determine the galactic latitude, b , of the galaxy and reject all galaxies with $|b| < b_{\text{lim}}$, where b_{lim} is the user-specified galactic latitude limit. The solid angle of the all-sky lightcone is then calculated as, $\Omega_{\text{all-sky}} = 4\pi - 2\pi [\sin(b_{\text{lim}}) - \sin(-b_{\text{lim}})]$.

where r_c is the maximum distance that light could have travelled in the time t , i.e. the maximum co-moving, radial distance that is visible to the observer. For a flat cosmology, i.e. with $\Omega_k = 0$, at the epoch corresponding to redshift, z , the maximum co-moving, radial distance, r_c , that is visible to an observer at the present day is given by,

$$r_c(z) = \int_0^z \frac{cdz'}{H_0 \sqrt{\Omega_m (1+z')^3 + \Omega_\Lambda}}, \quad (4)$$

where H_0 is the Hubble Constant at the present day, Ω_m is the matter density of the Universe and Ω_Λ is the vacuum energy density of the Universe but at the present day. To construct a mock galaxy catalogue, we place each halo at the epoch at which it enters the observer's past lightcone, i.e. the epoch at which the halo would first become "visible" to the observer. If this epoch corresponds to a redshift, z , then the halo is placed at the position, $\vec{r}(X, Y, Z, z)$, at which

$$|\vec{r}(X, Y, Z, z)| = r_c(z). \quad (5)$$

Each snapshot, i , in the *Millennium Simulation* corresponds to a discrete cosmic epoch, with redshift, z_i . To determine when a halo enters the lightcone, we loop over the simulation snapshots searching for the time-step during which Eq. (5) is satisfied. By comparing the position, $\vec{r}_j(X_j, Y_j, Z_j, z_i)$, of a halo j that exists at z_i to the maximum co-moving distance, $r_c(z_i)$, that is visible at that epoch, and doing the same for the descendant of the halo, labelled k , that exists at the next snapshot, $z_{i+1} < z_i$, we can determine whether halo j will enter the lightcone between the snapshots i and $i+1$, i.e. whether $z_{i+1} < z < z_i$.

Using $\vec{r}_j(X_j, Y_j, Z_j, z_i)$ and $\vec{r}_k(X_k, Y_k, Z_k, z_{i+1})$ as boundary conditions, we interpolate along the orbital path of the halo j to find the exact epoch, z , at which it enters the lightcone and the position, $\vec{r}_j(X, Y, Z, z)$, at which this occurs. We use a cubic polynomial to describe the position of the halo, in each Cartesian direction, as a function of the time t between the adjacent snapshots (i.e. $t_{i+1} < t < t_i$). For example, the Cartesian X component of the path is given by,

$$X(t) = A_X t^3 + B_X t^2 + C_X t + D_X, \quad (6)$$

where A_X , B_X , C_X and D_X are coefficients that can be determined by requiring that the boundary conditions ($X(t = t_i) = X_j(t_i)$, $X(t = t_{i+1}) = X_k(t_{i+1})$, $\dot{X}(t = t_i) = \dot{X}_j(t_i)$, $\dot{X}(t = t_{i+1}) = \dot{X}_k(t_{i+1})$) are satisfied. The X component of the velocity of the galaxy at time, t , is given by the derivative of Eq.(6) with respect to time. Equations similar to Eq.(6) can be derived for the $Y(t)$ and $Z(t)$ components. The centre of mass of the halo is then placed at $\vec{r}_j(X, Y, Z, z)$.

Our decision to use interpolation to determine halo positions is an extension of the method of Kitzbichler & White (2007), who explicitly chose not to use interpolation but instead placed halos according to the snapshot with the epoch closest to the one at which the halo enters the lightcone. Kitzbichler & White adopted this approach because of the difficulties inherent in using interpolation to predict realistic orbital paths for satellite galaxies. In the next section, we discuss these difficulties and suggest a solution that provides a good approximation for our purposes.

4.4.2 Placement of galaxies

The finite spatial extent of halos means that central and satellite galaxies within a halo will enter the lightcone at slightly different

times. Central galaxies are positioned on the most bound particle of the most massive `SUBFIND` group (see § 3.1.2) and are at rest relative to the halo. The location and time at which a central galaxy enters the lightcone is thus equal to that of its host halo and so for these galaxies we can use the calculation for the halo centre, as presented in §4.4.1. However, satellite galaxies can enter the lightcone at an earlier or later epoch than the centre of the host halo. When positioning a satellite galaxy we can still interpolate over the evolutionary path of its host halo, but we must first correct the spatial positions along the path to account for the relative offset between the position of the satellite galaxy and the centre of the halo. Therefore, we first need a model to describe the orbital path of a satellite within its host halo.

Modelling physically viable satellite orbits is a non trivial task. Difficulties arise when the large orbital velocities of satellite galaxies lead to orbital time-scales that are much shorter than the spacing of the simulation snapshots. Care must therefore be taken to ensure that numerical artefacts do not introduce large positional errors, which might in turn lead to inaccurate predictions for the one-halo term in the galaxy correlation function.

If, for example, we attempt to describe the orbital path of a satellite galaxy using a cubic polynomial in Cartesian space that is constrained to satisfy both the position and velocity boundary conditions, then in rare instances we may find that the large orbital velocities of satellite galaxies lead to orbital paths that are highly eccentric and extend out to large orbital radii. In the majority of cases where orbital velocities are small, the cubic function fits an orbital path similar to a simple linear interpolation scheme, which ignores the velocity boundary conditions. Example orbits, modelled using different interpolation schemes, are shown in Fig 2. Unfortunately, if a halo and its descendent are found on opposing sides of the halo centre of mass, then these interpolation schemes would lead to satellites being positioned much closer to the centre of mass of the halo than they should be. This would have the effect of boosting the clustering signal on small scales, as shown in the two left-hand panels of Fig 3.

Since measurements of galaxy clustering are integral for achieving many of the goals set by current and future galaxy surveys, we choose to prioritise the preservation of the galaxy clustering signal in real space. We do this by moving to a 2-dimensional (2D) plane, defined by the position of the halo centre of mass and the positions of the satellite, j , and its descendent, k , relative to the halo centre. By assuming that the orbit of satellite j is restricted to this plane, we use linear interpolation to express the change in the polar co-ordinates of the orbit of j (relative to the centre of mass of the halo, located at the origin) as a function of time between the snapshot epochs, $t_{i+1} < t < t_i$.

We describe the angular position, ϕ , of the satellite along its orbit as

$$\phi(t) = \phi_j(t_i) + [\phi_k(t_{i+1}) - \phi_j(t_i)] \left[\frac{t - t_i}{t_{i+1} - t_i} \right]. \quad (7)$$

A caveat is that we perform the interpolation along the path that corresponds to the smallest angular separation between the position of a satellite and its descendent, which may lead to satellites changing directions. To describe the change in the radius, ρ , of the orbit of the satellite we can choose to either linearly interpolate the radius in the same way, i.e.

$$\rho(t) = \rho_j(t_i) + [\rho_k(t_{i+1}) - \rho_j(t_i)] \left[\frac{t - t_i}{t_{i+1} - t_i} \right], \quad (8)$$

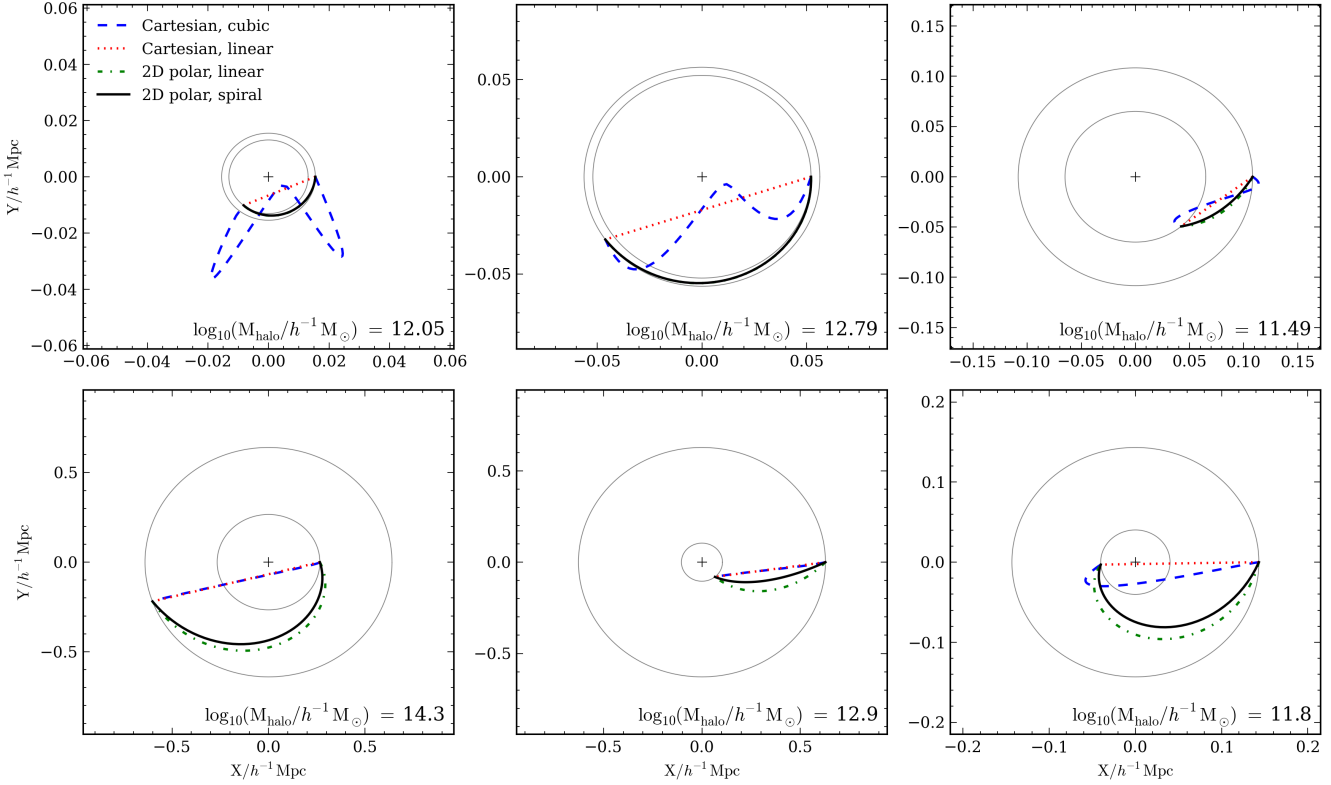


Figure 2. Examples demonstrating the modelling of the orbital paths of satellite galaxies between two adjacent simulation snapshots using different interpolation schemes. The positions of the satellite galaxies are displayed relative to the centre of mass of the halo, which is marked with a $+$. Circles show circular orbits at the start and end radii of the path of the satellite galaxy. The various interpolation schemes, which use either 3-dimensional Cartesian co-ordinates or 2-dimensional polar co-ordinates, are discussed in §4.4.2 and are shown using different line colours and styles, as indicated by the key in the top left panel. For the application presented in §5 we use the 2-dimensional polar, linear interpolation scheme.

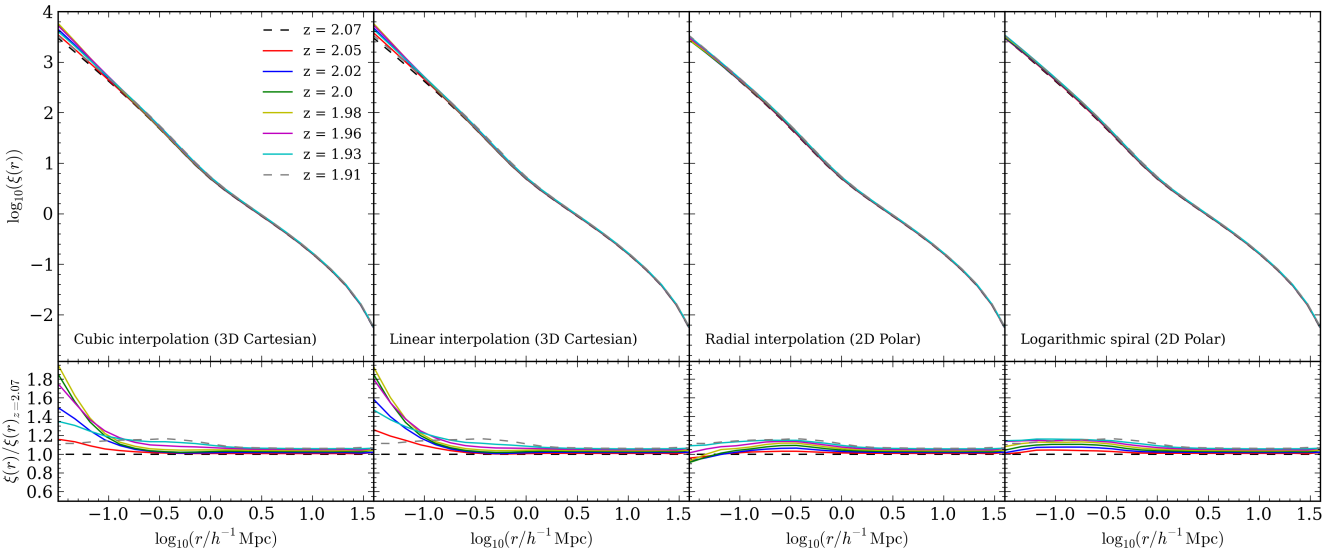


Figure 3. The real-space correlation function of galaxies predicted using four different satellite interpolation schemes: cubic interpolation in 3D Cartesian space (far left), linear interpolation in 3D Cartesian space (middle left), radial interpolation in 2D polar space (middle right) and modelling the satellite orbits using a logarithmic spiral in 2D polar space (far right). The upper panels show the correlation function for galaxies at two adjacent simulation snapshots (corresponding to redshifts $z = 1.91$ and $z = 2.07$, grey and black dashed lines) and the same galaxies at six intermediate redshifts (various solid, coloured lines). The lower panels show the ratio of each correlation function, relative to the correlation function measured at the $z = 2.07$ snapshot.

or couple the radius to the angle using a simple model, such as a logarithmic spiral,

$$\rho(t) = a \cdot e^{b \cdot \phi(t)}, \quad (9)$$

where $a = \rho_j(t_i)$ and $b = \phi_k(t_{i+1}) \ln(\rho_k(t_{i+1})/\rho_j(t_i))$. Note that in these two cases we are ignoring the velocity boundary conditions and assuming that $\dot{\rho}(t) = \dot{\phi}(t) = 0$. However, as can be seen in Fig 3, these methods preserve the galaxy clustering to smaller scales than possible with the 3-dimensional (3D) cubic or linear approaches. Note that in the above cases, we can interpolate the orbital velocities of satellites using the same equations as used for the positions. For the application in § 5, we have adopted to interpolate the satellite positions using Eq.(7) and Eq.(8), i.e. a 2-D polar linear interpolation of both the angle and radius of the satellite orbit.

By converting back to 3D Cartesian coordinates we can express the epoch, z , at which the satellite enters the lightcone as the position at which,

$$|\vec{r}_{\text{halo}}(X, Y, Z, z) + \vec{r}'_j(X, Y, Z, z)| = r_c(z), \quad (10)$$

where $\vec{r}_{\text{halo}}(X, Y, Z, z)$ is the global position of the dark matter hosting the satellite at this epoch and $\vec{r}'_j(X, Y, Z, z)$ is the position of the satellite relative to the centre of this halo.

Fig.3 shows that between $z = 1.91$ and $z = 2.07$ (which is a 5% change in $1 + z$) there is a 20% difference in the amplitude $\xi(r)$. If we did not interpolate the position of satellite galaxies between snapshots, then at a redshift intermediate to $z = 1.91$ and $z = 2.07$, there would be up to a $\sim 10\%$ error in the correlation function. Whilst any interpolation scheme is approximate, it is clear that it is better to make an attempt to adjust the galaxy positions if the lightcone crossing occurs between snapshots, rather than jumping from one set of fixed positions to the other, which would result in discontinuities in the correlation function.

4.5 Treatment of galaxy properties in the lightcone

4.5.1 Intrinsic properties

For each galaxy that enters the lightcone and satisfies the geometrical cuts described in §4.3, we need to output galaxy properties (i.e. stellar mass, SFR, etc.) that are appropriate for the epoch at which we have placed the galaxy.

With knowledge of the star-formation history of the galaxy, we can follow the evolution of any galaxy property over cosmic time. However, as with galaxy positions, this information is only recorded at the discrete epochs corresponding to the simulation snapshots. Ideally we would like to again use interpolation to determine the value for any galaxy property at any given epoch. Unfortunately the evolution of the majority of galaxy properties is complex and by interpolating between the snapshot epochs we risk oversimplifying this evolution and deriving incorrect values. For instance, the build-up of the stellar mass of a galaxy between two consecutive snapshots will receive contributions from many different sources. Besides quiescent star formation in the disk, many other events, such as disk instabilities or mergers with one or more other galaxies, can lead to starbursts and a SFR that is highly variable with time. In the case of galaxy mergers we cannot accurately say, from the snapshot data alone, when during a time-step the merger occurred. Therefore interpolation over the properties of each progenitor may lead to double counting and, at the epochs at which they enter the lightcone, each progenitor having properties that are (possibly significantly) mis-estimated.

We could evaluate galaxy properties for any given epoch by

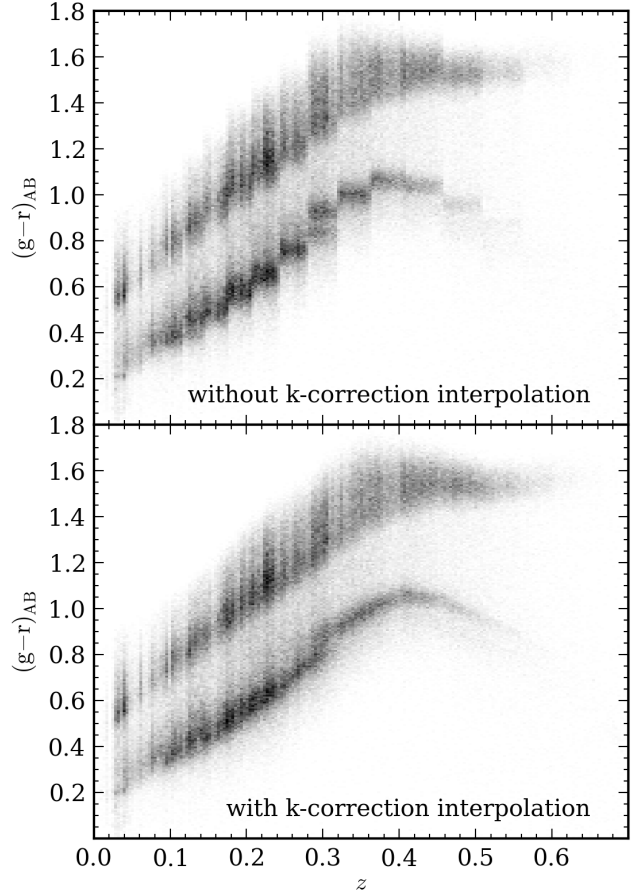


Figure 4. Distribution of SDSS $g - r$ colour as a function of redshift, z , in a lightcone catalogue constructed for the GAMA survey, both without k-correction interpolation (upper panel) and with k-correction interpolation (lower panel, see §4.5.2 for details). Shading corresponds to the number density of galaxies. (Note that the apparent vertical stripes in the galaxy distributions correspond to peaks in the galaxy redshift distribution.)

solving the set of coupled differential equations that govern the exchange of material between the hot gas in the halo and the cold gas and stars in the galaxy. However, this exercise is non-trivial and would require the full calculation performed by GALFORM to be reproduced for each galaxy out to the epoch at which it enters the lightcone, which would be computationally expensive. Similarly, we could have originally run GALFORM and output the galaxy properties on a finer time mesh. However, this would extend the run time of the model and take up significantly more disk space. Instead, we adopt a procedure similar to that of Kitzbichler & White (2007) and, for any galaxy that enters the lightcone, we assign the galaxy the intrinsic properties it had at the snapshot immediately prior to the epoch, z , at which it entered the lightcone, i.e. the snapshot i with the smallest redshift, z_i , for which $z_i > z$.

4.5.2 Observed properties

Having set the intrinsic properties of the galaxies, we can now use this information, along with their positions, to evaluate their observed properties, namely their observed fluxes (and apparent magnitudes). At this point we need to use the position of a galaxy to derive its luminosity distance, d_L , which is required to relate the emit-

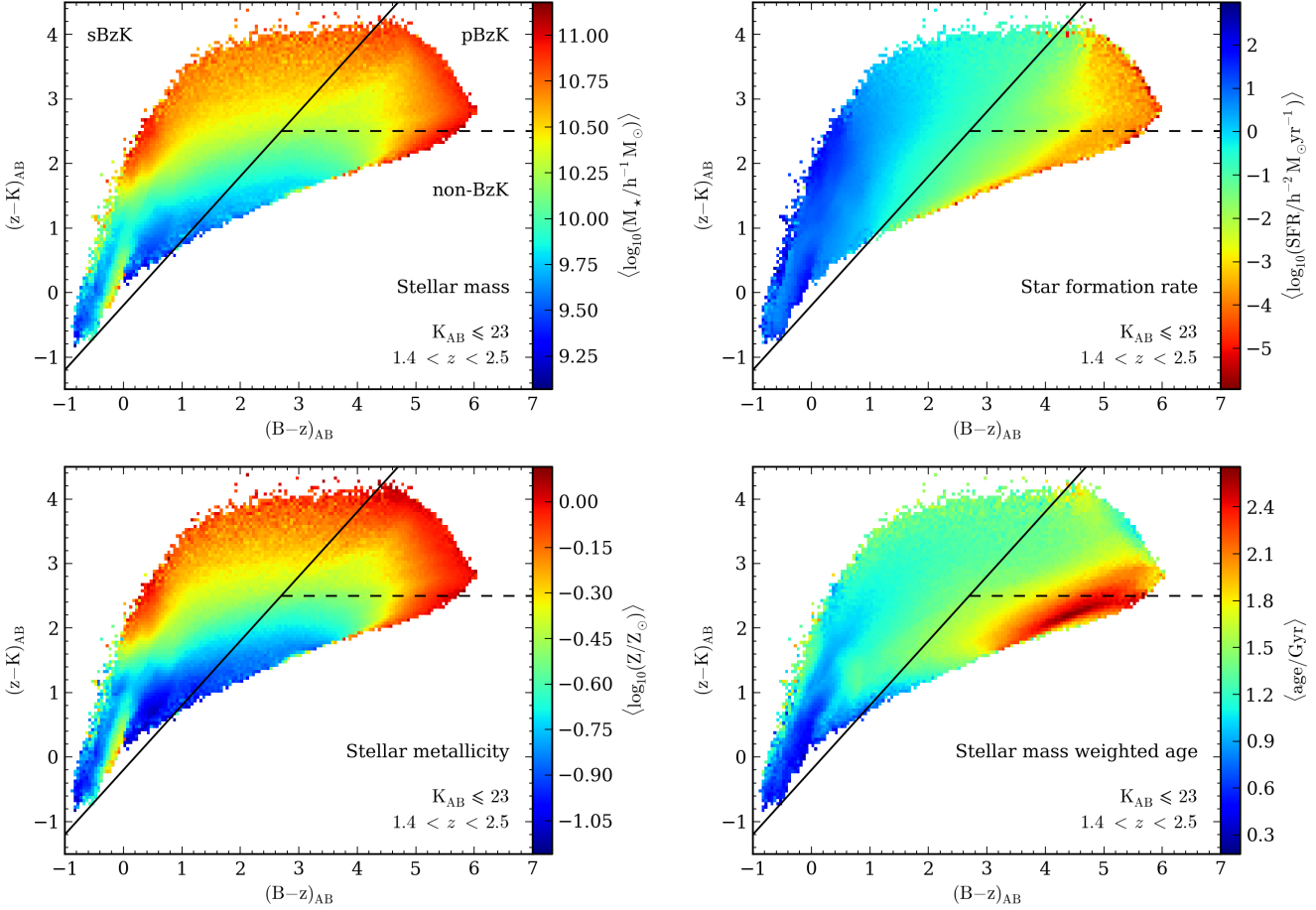


Figure 5. The predicted distribution of $K_{AB} \leq 23$ galaxies with $1.4 < z < 2.5$ in the BzK colour plane, colour coded, as indicated by the key on the right of each panel, according to the median value in a 2-dimensional colour-colour bin for different galaxy properties: stellar mass (upper left), star-formation rate (upper right), stellar metallicity (lower left) and stellar mass weighted age (lower right). The solid and dashed lines correspond to the BzK criteria used by Daddi et al. (2004a) (see 5.1 for further details). The sBzK and pBzK regions have been labelled in the upper left panel.

ted luminosity per unit frequency, $L_\nu(\nu_e)$, of an object to its observed flux per unit frequency, $S_\nu(\nu_o)$. For a flat Universe the luminosity distance out to a redshift z is simply, $d_L(z) = r_c(z)(1+z)$. Therefore a galaxy in the lightcone at a cosmological redshift z will have an observed flux,

$$S_\nu(\nu_o) = (1+z) \frac{L_\nu(\nu_e)}{4\pi d_L^2(z)}, \quad (11)$$

where ν_o is the observed frequency of the light from the galaxy. The emitted (rest-frame) frequency is related to the observed (observer-frame) frequency by $\nu_e = \nu_o(1+z)$. The observer-frame apparent magnitude of a galaxy, in the AB system, is then given by,

$$m_{AB} = -2.5 \log_{10} \left[\frac{\int S_\nu(\nu_o) R(\nu_o) d\nu_o}{S_{\nu_o} \int R(\nu_o) d\nu_o} \right], \quad (12)$$

where $R(\nu_o)$ is the filter response of a specified photometric band and S_{ν_o} is the AB reference flux per unit frequency (Oke & Gunn 1983).

In our case, GALFORM calculates the emitted luminosity of a galaxy, so we can calculate the observer-frame absolute magnitude, M_{AB} , of the galaxy (assuming $z \neq 0$) from,

$$M_{AB} = -2.5 \log_{10} \left[\frac{\int L_\nu(\nu_e) R\left(\frac{\nu_e}{1+z}\right) d\nu_e}{L_{\nu_o} \int R\left(\frac{\nu_e}{1+z}\right) d\nu_e} \right], \quad (13)$$

where L_{ν_o} is now the AB reference luminosity, $L_{\nu_o} = 4\pi(10\text{pc})^2 S_{\nu_o}$. From this we can calculate the observer-frame apparent magnitude of a galaxy, in the AB system, by,

$$m_{AB} = M_{AB} + 5 \log_{10} \left(\frac{d_L(z)}{10\text{pc}} \right) - 2.5 \log_{10} (1+z). \quad (14)$$

Due to the large number of galaxies modelled by GALFORM, the full SED of each galaxy is not stored. Instead, the luminosity is computed in a set of filters specified at run time. Hence the definition of the filter response in the galaxy rest frame, $R(\nu_e/(1+z))$, is tied to the output redshifts of the simulation snapshots and the k-correction applied does not correspond to the redshift of the galaxy in the lightcone. This discrepancy leads to visible discontinuities in distributions involving the photometric properties of the galaxies, such as galaxy colours versus redshift, as shown in the upper panel of Fig. 4. The breaks apparent in the distribution correspond to the redshifts of the simulation snapshots.

As discussed in the previous section, the complex time dependence of galaxy luminosity means that we cannot simply interpolate the absolute magnitudes. However, since the size of the

wavelength shift applied to a filter depends only on the redshift to the galaxy (and not on any of its intrinsic properties), then we can apply a correction to all the observer-frame absolute magnitudes (and dust emission luminosities) to take into account the redshift of lightcone crossing. Consider again a galaxy, j , that is originally found in the snapshot, i , at redshift z_i , and which has a descendent in snapshot $i + 1$, at a redshift $z_{i+1} < z_i$. Assume that the galaxy has an observer-frame absolute magnitude $M_j(z_i)$. Since the wavelength shift applied depends only on the redshift of a galaxy, we can easily predict the observer-frame absolute magnitude that j would have if placed at the redshift of its descendent in snapshot $i + 1$, i.e. $M_j(z_{i+1})$ within the GALFORM code, but with a star-formation history computed up to t_i . If the galaxy, j , enters the lightcone at an intermediate epoch, z , then we can interpolate between $M_j(z_i)$ and $M_j(z_{i+1})$ to estimate $M_j(z)$. Note that by interpolating the magnitudes (and luminosities) in this way, we have not changed the shape of the SED of the galaxy, but rather have applied a further systematic wavelength shift to the galaxy SED. As can be seen in the lower panel of Fig. 4, this correction, which was also applied by Blaizot et al. (2005) and Kitzbichler & White (2007), smooths out the ‘saw-tooth’ pattern seen in the colour distribution.

We can also calculate an observed redshift for the mock galaxies, emulating the measurement that would be taken from a galaxy spectrum using one or more identified emission lines. The observed redshift, z_{obs} , of a galaxy, which includes the cosmological redshift due to the Hubble flow as well as a component due to the local peculiar motion of the galaxy, is defined by,

$$z_{\text{obs}} = (1 + z) \left(1 + \frac{v_r}{c} \right) - 1, \quad (15)$$

where z is the cosmological redshift at which the galaxy enters the lightcone and v_r is the radial component of the peculiar velocity vector, \vec{v} , of the galaxy (i.e. $v_r = \vec{v} \cdot \hat{r}$, where \hat{r} is the normalised line-of-sight position vector of the galaxy). We do not at present include any calculation of photometric redshifts, or their uncertainties, in GALFORM or our lightcone code. These properties can be readily calculated in post-processing using the photometry output for each galaxy.

4.6 Applying the survey criteria

The final stage in constructing a mock catalogue is to apply the radial selection criteria of the survey being mimicked and reject those galaxies fainter than the specified flux limits. For many surveys this involves placing a cut on the flux at one or more wavelengths or an apparent magnitude limit in one or more photometric bands. We can select galaxies according to any intrinsic or observed galaxy property. For example, besides generating flux limited lightcone catalogues, we are able to construct catalogues limited by stellar mass, atomic hydrogen mass or even halo mass. Given a list of selection criteria, we can control whether a galaxy must pass just one or all of these criteria simultaneously in order to be included in the final catalogue. Note that the lightcone catalogues that we produce correspond to ideal surveys, i.e. we do not apply any completeness masks or simulate the loss of galaxies due to poor observing conditions, fibre collisions or quality of spectra. Such completeness effects are survey specific and can be applied to the catalogues in post-processing.

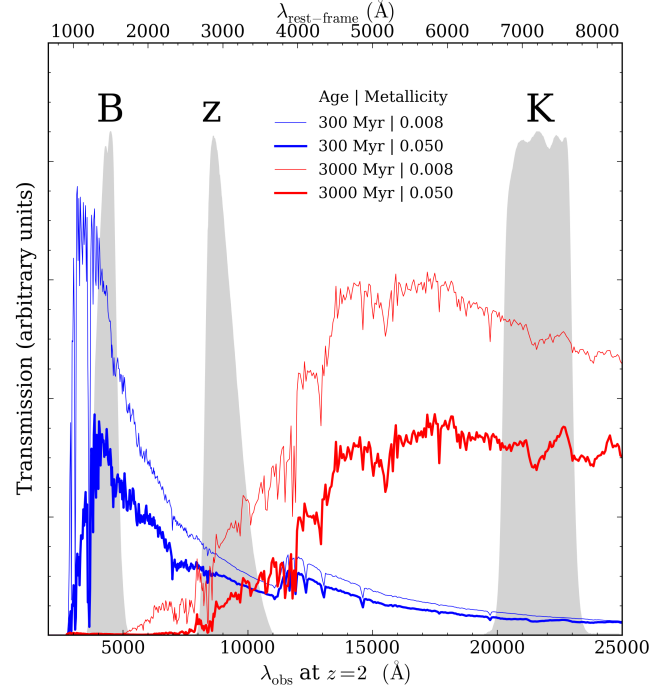


Figure 6. The shading shows the transmission curves of the B, z and K filters used by Daddi et al. (2004a). Also shown are the synthetic spectra (plotted as luminosity per unit wavelength) for two galaxies at $z = 2$. The spectra were obtained using PEGASE.2 (Fioc & Rocca-Volmerange 1999), assuming a Kennicutt (1983) IMF, and a single instantaneous burst of star formation. The spectra are shown for two different epochs, when the stellar population has an age of 300 Myr (blue) and an age of 3000 Myr (red) and for a sub-solar (thin line) and a super-solar (thick line) metallicity. The flux and transmission units are arbitrary and the spectra have been normalised so as to be visible on similar scales to the transmission curves.

5 APPLICATION TO THE BzK COLOUR SELECTION

In this section we use a lightcone mock catalogue of 50 deg^2 , built using the Bower et al. (2006) GALFORM model, to study the properties of galaxies selected using the BzK colour technique. We have constructed the lightcone by selecting all galaxies with $K_{\text{AB}} \leq 24$.

5.1 The BzK selection

The BzK colour selection is designed to identify galaxies in the redshift interval $1.4 < z < 2.5$ based upon their location in the $(B - z)$ vs. $(z - K)$ colour plane (Daddi et al. 2004a). Additionally, the selection is also advertised as being able to separate star-forming galaxies from those that are passively evolving.

Daddi et al. identified star-forming galaxies at $z > 1.4$ (referred to as star-forming BzK, or sBzK galaxies) using the criterion

$$\text{BzK} \geq -0.2, \quad (16)$$

where $\text{BzK} \equiv (z - K)_{\text{AB}} - (B - z)_{\text{AB}}$. This condition is indicated by the solid black line in Fig. 5. The sBzK region lies above this line, as labelled in the upper left panel of Fig. 5.

To select galaxies at $z > 1.4$ that are passively evolving (referred to as passive BzK, or pBzK galaxies)⁷, Daddi et al. proposed applying the following conditions:

$$\text{BzK} < -0.2 \text{ and } (z - K)_{\text{AB}} > 2.5. \quad (17)$$

The pBzK galaxies populate the region between the solid and dashed lines in Fig. 5, i.e. the upper right region of the $(B - z)$ vs. $(z - K)$ colour plane.

The BzK selection works by using colours that sample key features in the spectral energy distributions of galaxies at $1.4 < z < 2.5$, mainly the rest-frame 4000\AA break and the UV continuum slope. Fig. 6 shows the synthetic spectra for two galaxies at $z = 2$, obtained using the PEGASE.2 stellar population synthesis code (Fioc & Rocca-Volmerange 1999). The red lines correspond to a galaxy that is dominated by an old stellar population and thus exhibits a prominent break around 4000\AA (in the rest frame), which is created by the build-up of the absorption lines of ionised metals. Between $1.4 < z < 2.5$ the break moves over the observed wavelength range $\sim 9000 - 15000\text{\AA}$, between the z- and K-bands. In this redshift range, we find that the $(z - K)$ colours of model galaxies become monotonically redder with increasing strength of the 4000\AA break.

At $z \leq 1.4$, the continuum longwards of the 4000\AA break is shifted into the z-band, resulting in galaxies at these redshifts having bluer $(z - K)$ colours (and, for a fixed B-band flux, redder $(B - z)$ colours). The BzK criteria are therefore designed to exclude these galaxies, which lie to the right of the solid line and below the dashed line in Fig. 5. However, as we will see in § 5.4, the finite width of both the break and the z-band filter, mean that we would expect some contamination to occur, as well as the loss of some galaxies within the target redshift interval, $1.4 < z < 2.5$.

As can be seen in Fig. 6, the 4000\AA break is stronger for galaxies with old stellar populations or high stellar metallicity (Kauffmann et al. 2003; Kriek et al. 2006, 2011). As such, we would expect old, metal rich galaxies to display redder $(z - K)$ colours. The lower two panels in Fig. 5 show the predicted variation of metallicity (left) and stellar mass weighted age (right) within the $(B - z)$ vs. $(z - K)$ plane. The predicted trends with $(z - K)$ colour agree with the expectations for the variation of the 4000\AA break with both age and metallicity. However, these trends are weakened by the effect of dust in young galaxies, which reddens the $(z - K)$ colour.

To isolate young, metal poor galaxies at $1.4 < z < 2.5$ that have not yet developed a strong 4000\AA break, another spectral feature is required. Young, star-forming galaxies have steep UV continua due to the presence of bright, young, hot stars. At $z \sim 2$ the UV continuum is shifted into the optical, as shown in Fig. 6. The presence of the steep UV slope boosts the B-band flux of these galaxies, leading them to have very blue $(B - z)$ colours, as can be seen in the lower right panel of Fig. 5. The correlation between UV luminosity, due to young stars, and star-formation rate, SFR, suggests that we would also expect a correlation between the SFR of a galaxy and its $(B - z)$ colour for a given K-band limit. Such a trend is clearly visible in the upper right panel of Fig. 5.

5.2 Predicted numbers of BzK galaxies

Since the BzK technique is used to select a subsample of K-band (or B-band) selected galaxies, we first inspect the predicted total number counts of all galaxies in the B and K-bands in the mock catalogue, which are shown by the solid lines in Fig. 7. We remind the reader that our mock catalogue has a solid angle of 50 deg^2 and that galaxies were selected with $K_{\text{AB}} \leq 24$. In both bands, the GALFORM mock catalogue provides a reasonable match to the observed counts. The B-band counts are in excellent agreement with the observed numbers, though turn over at $B_{\text{AB}} \sim 25$ due to the $K_{\text{AB}} \leq 24$ selection used to construct the lightcone.

As a sanity check, the dotted lines in Fig. 7 show the differential number counts obtained by integrating the GALFORM galaxy luminosity function over co-moving volume. The excellent agreement between the counts computed using the luminosity functions directly from the snapshot outputs and those from the lightcone demonstrates the success of the magnitude interpolation scheme used to create the lightcone. The light grey shaded region in Fig 7 shows the spread (10 to 90 percentile range) in the counts for 100 separate fields each with a solid angle of 1 deg^2 , a solid angle typical for the observational datasets we are comparing. These fields were generated by randomly selecting field centres within the footprint of the lightcone, with a buffer zone to avoid placing field centres too close to the edge of the footprint. In the right-hand panel of Fig. 7, the counts computed from the luminosity function diverge from the predicted counts in the lightcone due to the K-band limit used to construct the lightcone (whereas the integral over the luminosity function is independent of this limit).

In the left-hand panel of Fig. 8 we show the number counts of all BzK galaxies with $K_{\text{AB}} \leq 24$ from the mock catalogue (solid line). Overall the mock provides a reasonable match to the observed counts. At faint magnitudes ($K_{\text{AB}} \gtrsim 22$), the turnover in the observed BzK counts is sharper than predicted. However, in this region the observations could be incomplete. The closest agreement between the predictions and observations occurs for $K_{\text{AB}} \sim 20.5 - 22.0$, where there is a clear change of slope in both the observations and the GALFORM predictions. At $K_{\text{AB}} \sim 21$, $\sim 1/6$ of both observed and predicted K-band selected galaxies are also BzK galaxies. Brightwards of $K_{\text{AB}} \sim 19.5$, the predicted BzK counts exceed the counts for K-band selected galaxies within $1.4 < z < 2.5$ (shown by the dotted line) due to low redshift interlopers (see § 5.4.2). In Fig. 8, the light grey shaded region again shows the 10 - 90 percentile spread in the differential number counts of BzK selected galaxies in 100 separate fields, each with a solid angle of 1 deg^2 . At bright magnitudes, the extent of this shaded region indicates that the spread in the observed counts can be explained as sampling variance arising from the small solid angles probed.

We now consider the predicted number counts for the subsamples of sBzK and pBzK galaxies, shown in the middle and right panels of Fig. 8. For faint fluxes ($K_{\text{AB}} \gtrsim 21$), sBzK galaxies, both observed and predicted, dominate the BzK population due to the turnover in the pBzK counts that can be clearly seen in the right-hand panel of Fig. 8.

The GALFORM sBzK number counts show a good overall agreement with the observations. However, the model over-predicts the number of the faintest sBzK galaxies. This may simply be the result of the observed sBzK counts becoming incomplete at faint magnitudes. The predicted number counts of pBzK galaxies are in reasonable agreement with observations in the range $19.8 \lesssim K_{\text{AB}} \lesssim 20.8$. However, the model under-predicts the

⁷ We shall refer to the combined sBzK and pBzK galaxy population as BzK galaxies.

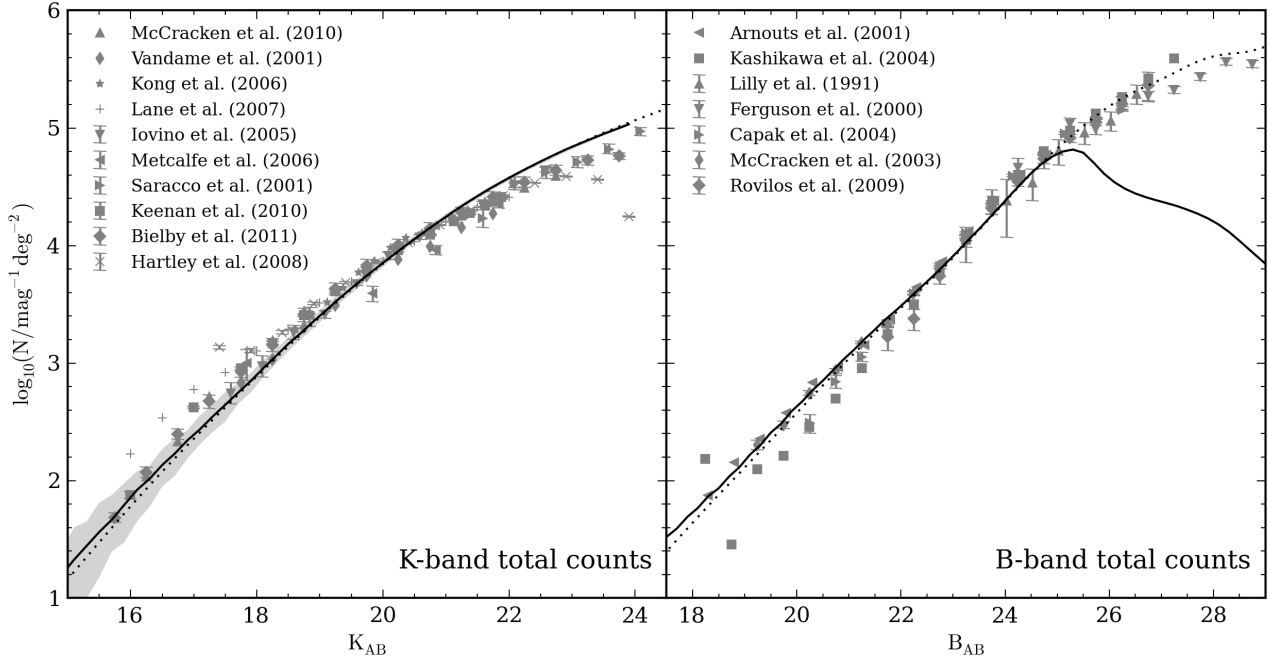


Figure 7. Predicted K_{AB} -band (left) and B_{AB} -band (right) differential number counts for all $K_{AB} \leq 24$ selected galaxies in the lightcone constructed using the Bower et al. (2006) model (solid lines). The dotted lines show the number counts calculated by integrating the GALFORM galaxy luminosity function over co-moving volume. The latter uses a single band limit, hence the discrepancy with the counts from the lightcone in the B-band. Also shown are observationally estimated K-band number counts from Saracco et al. (2001); Vandame et al. (2001); Iovino et al. (2005); Metcalfe et al. (2006); Kong et al. (2006); Lane et al. (2007); Hartley et al. (2008); Keenan et al. (2010); McCracken et al. (2010); Bielby et al. (2011) and B-band number counts from Lilly et al. (1991); Ferguson et al. (2000); Arnouts et al. (2001); McCracken et al. (2003); Kashikawa et al. (2004); Capak et al. (2004); Rovilos et al. (2009). In the left-hand panel, the light grey shaded region shows the 10 – 90 percentile spread in the K_{AB} -band differential number counts for 100 separate 1 deg^2 lightcone fields.

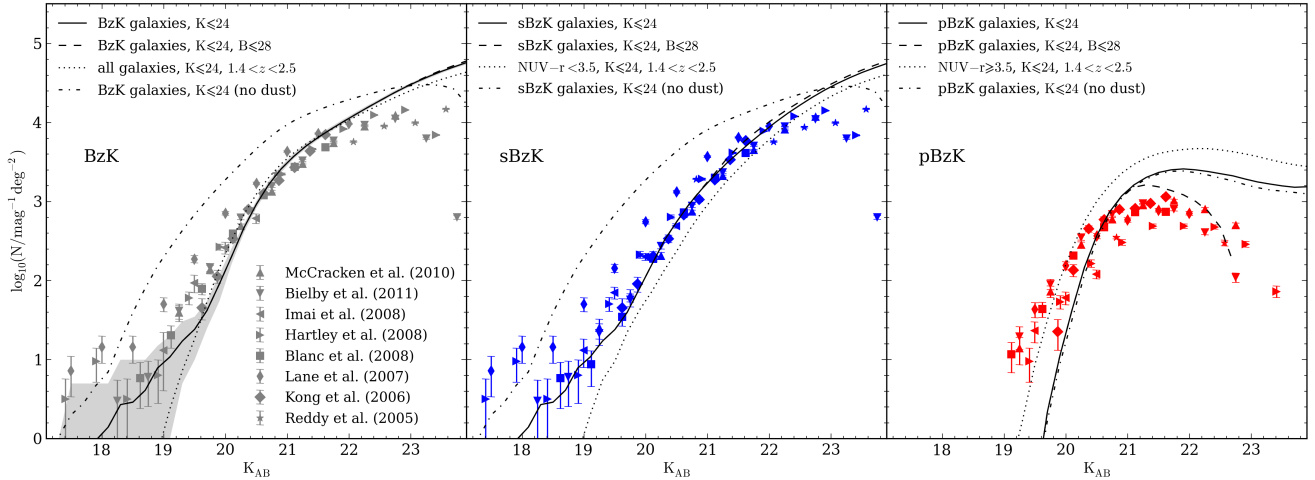


Figure 8. Predicted K_{AB} -band differential number counts for all BzK (left), sBzK (middle) and pBzK selected galaxies (right) with $K_{AB} \leq 24$ in the lightcone catalogue (solid lines). The dashed lines show the predicted number counts when a B-band detection limit of $B_{AB} \leq 28$ is considered in addition to the K-band limit (see § 5.2, in the left-hand panel, this line is underneath the solid one). The dot-dashed lines show the BzK number counts when extinction due to dust is omitted (see §5.5.5). In the left-hand panel, the dotted line shows the counts for all $K_{AB} \leq 24$ selected galaxies within $1.4 < z < 2.5$. In the middle panel the dotted line corresponds to the counts of galaxies with $NUV - r < 3.5$, $K_{AB} \leq 24$ and $1.4 < z < 2.5$ and in the right-hand panel the dotted line corresponds to the counts of galaxies with $NUV - r \geq 3.5$, $K_{AB} \leq 24$ and $1.4 < z < 2.5$ (see § 5.2 for further details on the colour cut). Also shown are observationally estimated number counts from Reddy et al. (2005); Kong et al. (2006); Lane et al. (2007); Blanc et al. (2008); Hartley et al. (2008); Imai et al. (2008); McCracken et al. (2010); Bielby et al. (2011). In the left-hand panel, the light grey shaded region shows the 10 – 90 percentile spread in the K_{AB} -band differential number counts of BzK galaxies in 100 separate 1 deg^2 lightcone fields.

number of brighter pBzK galaxies and over-predicts the number of fainter galaxies. This mismatch between semi-analytical predictions and observed pBzK number counts has previously been shown by McCracken et al. (2010), who compared their observational counts to the predictions of the mock catalogues of Kitzbichler & White (2007). Moreover, the Kitzbichler & White model gave a poorer match to the observed sBzK counts than we find.

The turnover at faint magnitudes in the counts of pBzK selected galaxies has been reported by several authors (e.g. Lane et al. 2007; Hartley et al. 2008; McCracken et al. 2010; Bielby et al. 2011). The model also displays a turnover in the pBzK counts, but at $K_{AB} \sim 21$, ~ 1 mag fainter than in the data. Both Hartley et al. (2008) and McCracken et al. (2010) propose that limited B-band photometry is responsible for the turnover. Hartley et al. showed that reclassifying ~ 34 per cent of their sBzK galaxies as pBzK galaxies, would be sufficient to remove the turnover (we will return to this point in § 5.4.3). We demonstrate the impact of the depth of the B-band photometry by recalculating the predicted counts of BzK, sBzK and pBzK galaxies assuming a B-band detection limit of $B_{AB} = 28$ in addition to the K-band limit of $K_{AB} \leq 24$. Any galaxy in the mock catalogue with a B-band magnitude fainter than this is assumed to be undetected in B and its $(B - z)$ colour is calculated assuming $B_{AB} = 28$. This is the approach typically used in observational catalogues to estimate the colours of objects that are undetected in a band. The effect this has on the counts is shown by the dashed lines in Fig. 8. Although the predicted pBzK counts are still not in full agreement with the data, applying a B-band limit has reduced the mismatch. With the B-band limit applied, ~ 50 per cent of the pBzK galaxies are relabelled as sBzK galaxies preferentially at the faintest K-band magnitudes. This supports the conclusion that shallow B-band photometry contributes to the turnover. Hartley et al. and McCracken et al. both observed the turnover for K-band limited samples down to $K_{AB} \leq 23.5$ and $K_{AB} \leq 23$ respectively, with B-band detection limits of $B_{AB, \text{lim}} = 28.4$ and $B_{AB, \text{lim}} = 29.1$ respectively. The predicted excess of faint pBzK galaxies is also partially a result of the Bower et al. (2006) model predicting too many red galaxies. A substantial fraction of pBzK galaxies are satellites. These galaxies could be too red due to the treatment of gas stripping in satellite subhalos (see Font et al. 2008). If we plot the predicted pBzK number counts considering only central galaxies (without applying any B-band detection limit), we find that the predicted excess of faint pBzK galaxies is reduced, leading to excellent agreement with the observed counts.

The BzK criteria is not the only technique used observationally to classify galaxies as star-forming at $z \sim 2$. The rest-frame near-UV/optical colour, $\text{NUV} - r$, can also be used to separate star-forming and passive galaxies. Following Ilbert et al. (2010), we divide the K-band selected GALFORM galaxies lying within $1.4 < z < 2.5$, into star-forming galaxies (i.e. those with $\text{NUV} - r < 3.5$) and passively evolving galaxies ($\text{NUV} - r \geq 3.5$) and calculate their number counts. As shown in the middle panel of Fig. 8, the predicted sBzK counts are consistently somewhat higher than those predicted for galaxies with a blue $\text{NUV} - r$ colour in $1.4 < z < 2.5$. We note, however, that low-redshift contamination will exaggerate the counts in the brightest bins. The predicted number counts of pBzK galaxies are systematically below the counts of passive galaxies estimated using the $\text{NUV} - r$ colour. This highlights the sensitivity of the separation of galaxies into star-forming and passively evolving classes to the precise colour criteria used.

The mock catalogue is able to reproduce the combined number counts of all BzK galaxies, as well as providing reasonable

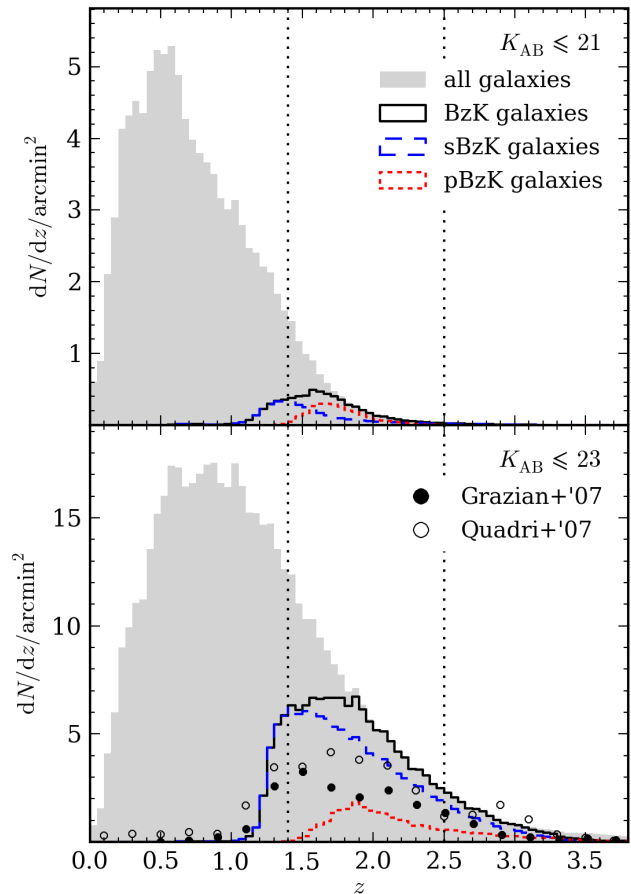


Figure 9. The predicted redshift distributions of BzK selected galaxies in the mock catalogue (black solid line) for two different K-band flux limits: $K_{AB} \leq 21$ (top) and $K_{AB} \leq 23$ (bottom). For comparison, the redshift distribution of all K-band selected mock galaxies down to these limits is shown by the grey shaded region. The limits of the redshift range which the BzK technique was designed to probe are indicated by the vertical dotted lines. Blue dashed and red dotted histograms show the redshift distributions of sBzK and pBzK galaxies respectively. In the bottom panel are plotted observed redshift distributions for BzK galaxy samples with $K_{AB} \leq 23.8$ and $K_{AB} \leq 22.9$ from Grazian et al. (2007) and Quadri et al. (2007) respectively.

agreement with the counts of K-band selected galaxies within $1.4 < z < 2.5$. Although the model is able to reproduce the predicted number counts of sBzK galaxies (which dominate the BzK population), it is unable to reproduce the predicted number counts of pBzK galaxies.

5.3 Predicted redshift distribution of BzK galaxies

In Fig. 9 we show the predicted redshift distributions for BzK galaxies in the GALFORM mock catalogue for two example K-band flux limits, $K_{AB} \leq 21$ and 23 . For comparison, we also show the redshift distribution for all model galaxies brighter than the stated K-band limit, and use vertical dotted lines to indicate the redshift range which the BzK technique is designed to probe, $1.4 < z < 2.5$.

It is clear from Fig. 9 that BzK galaxies probe the high-redshift tail of the redshift distribution of K-selected galaxies. For ex-

ample, the predicted median redshift of the $K_{AB} \leq 23$ sample is $z_{\text{med}} \sim 1.2$, while the BzK subsample has a higher median redshift of $z_{\text{med}} \sim 1.9$. Moreover ~ 98 per cent of the GALFORM galaxies within $2.0 \lesssim z < 2.5$ are selected as BzK galaxies. However, in the redshift range $1.4 < z \lesssim 2$, the fraction of galaxies selected by the BzK technique decreases with decreasing redshift. For $K_{AB} \leq 21$ the fraction of galaxies at $z = 1.4$ that are recovered is $\sim 20 - 25$ per cent, compared to ~ 50 per cent for $K_{AB} \leq 23$. For $K_{AB} \leq 21$ the fraction of galaxies recovered reaches 50 per cent at $z \sim 1.55$.

In the lower panel of Fig. 9 we compare the redshift distribution for our BzK selected galaxy sample with observed photometric redshift distributions from Grazian et al. (2007) and Quadri et al. (2007), selected with $K_{AB} \leq 23.8$ and $K_{AB} \leq 22.9$ respectively. The predicted BzK redshift distribution has a median redshift, $z_{\text{med}} \simeq 1.8$, that is consistent with the median redshifts of the observed distributions, $1.7 \lesssim z_{\text{med}} \lesssim 1.9$. As we have seen in the left-hand panel of Fig. 8, the GALFORM model over-predicts the number counts of BzK galaxies at $K_{AB} = 23$ and so, understandably, for all redshift bins within $1.4 < z < 2.5$, the mock catalogue predicts a greater number of BzK galaxies than is observed.

We can see from Fig. 9 that the redshift distribution of sBzK galaxies consistently peaks at lower redshifts than the pBzK distribution. This can also be seen in Fig. 10, which shows the predicted large-scale distribution of $K_{AB} \leq 21$ predicted galaxies and the subsamples of sBzK and pBzK galaxies. Fig. 10 shows that, while sBzK galaxies can be selected at redshifts down to $z \sim 0$, pBzK galaxies only start to appear at $z \sim 1.4$. In Fig. 10 we can also see that at $z \sim 2$ the pBzK galaxies appear to trace filamentary structures compared to the sBzK galaxies, which appear to be less clustered. Only for fainter limits of $K_{AB} \lesssim 23$, do sBzK galaxies begin to trace the filamentary structure at $z \sim 2$. This suggests that the predicted spatial clustering of pBzK galaxies is stronger than that for sBzKs, in agreement with observations (e.g. Kong et al. 2006; Hartley et al. 2008).

5.4 Efficiency of the BzK selection

The BzK technique was designed to select galaxies within $1.4 < z < 2.5$ and to separate them into star-forming and passively evolving subsamples. To assess the effectiveness with which the BzK technique achieves these goals, we consider the completeness (§ 5.4.1) and contamination (§ 5.4.2) of a BzK galaxy sample selected from the GALFORM mock catalogue.

5.4.1 K-band completeness

In this section we explore the fraction of K-band selected galaxies at $1.4 < z < 2.5$ that are actually picked up when using the BzK selection technique for galaxies in the GALFORM mock catalogue. For this purpose we compare the predicted number counts of BzK galaxies, presented in the left-hand panel of Fig. 8, with the total number counts of K_{AB} -band selected galaxies that lie within the target redshift range, shown by the dotted line in the same panel of Fig. 8. Faintwards of $K_{AB} \sim 19.5$ the predicted BzK counts are in good agreement with the counts of $1.4 < z < 2.5$ galaxies, indicating that the BzK selection is an effective probe of the galaxy population at this epoch.

In Fig. 11 we show the $(B - z)$ vs. $(z - K)$ plane populated by GALFORM galaxies within three different redshift regimes, $z \leq 1.4$ (left column), $1.4 < z < 2.5$ (middle column) and $z \geq 2.5$ (right column). The distribution is shown for our two example K-band flux limits: $K_{AB} \leq 21$ (top row) and $K_{AB} \leq 23$

(bottom row). We define the completeness of the BzK technique as the fraction of all galaxies in $1.4 < z < 2.5$ that lie in either of the BzK regions in the $(B - z)$ vs. $(z - K)$ plane. About a quarter of the galaxies brighter than $K_{AB} = 21$ within $1.4 < z < 2.5$ lie outside of the BzK regions. The distribution has two clear peaks, one at $(B - z) \sim 0$, which we will refer to as the star-forming peak, and the other at $(B - z) \sim 5$, which we will refer to as the passively evolving peak. The star-forming peak falls well within the sBzK region, while the passively evolving peak lies just outside the pBzK region. This would explain the under-prediction of the pBzK number counts for $K_{AB} \lesssim 20$. However, for $K_{AB} \leq 23$, the star-forming peak dominates the galaxy population suggesting that for fainter K-band limits the BzK selection provides a more complete sample of the $1.4 < z < 2.5$ galaxy population.

The completeness of the BzK technique, as a function of the limiting K-band magnitude of the galaxy sample, is shown in Fig. 12. Here, the data points show the BzK completeness estimates from Bielby et al. (2011), who applied the BzK selection to an input catalogue of ~ 1.8 million K-band galaxies, with photometric redshifts ($\sigma_{\Delta z/(1+z)} \lesssim 0.03$), from the WIRCam Deep Survey (WIRDS). We can clearly see in Fig. 12 that the BzK completeness increases with fainter K-band limiting magnitude. The same trend is seen for the completeness predictions for GALFORM galaxies, shown by the solid line, with ~ 55 , ~ 73 and ~ 80 per cent of $1.4 < z < 2.5$ galaxies being recovered for $K_{AB} \leq 21$, 22 and 23 respectively. Therefore, for faint K-band limits ($K_{AB, \text{lim}} \gtrsim 22$), the BzK technique is consistently selecting 75 to 80 per cent of the galaxies within $1.4 < z < 2.5$. However, for a very bright limit of $K_{AB} \leq 20$ the technique identifies less than half of the galaxy population within the target redshift range. For $21 \lesssim K_{AB, \text{lim}} \lesssim 22$ the completeness estimates from the GALFORM mock catalogue are in very good agreement with the WIRDS estimates.

5.4.2 Contamination

We now explore the predicted numbers of galaxies outside the redshift range, $1.4 < z < 2.5$, that are picked up by the BzK selection. As we can see from Fig. 11, it is not possible to ever have a sample of BzK selected galaxies that is entirely free of contamination from interlopers with low, $z \leq 1.4$, or high redshift, $z \geq 2.5$, which are classified as BzK galaxies. The left-hand column of Fig. 11 shows that low redshift interlopers are typically classified as sBzK galaxies, while the $(z - K)$ cut used in Eq. 17 successfully eliminates low redshift pBzK galaxies. High redshift interlopers, shown in the right-hand column of Fig. 11, appear to be more evenly distributed between the sBzK and pBzK regions and thus more difficult to remove.

The fractions of low and high redshift interlopers, as a function of K-band limiting magnitude, are shown in Fig. 12 by the dashed and dotted lines respectively. From Fig. 12 we can see that by applying a bright $K_{AB} \leq 20$ selection to our GALFORM mock catalogue, the BzK technique selects approximately equal numbers of galaxies with $1.4 < z < 2.5$ and $z \leq 1.4$. Pushing the K-band selection limit to fainter magnitudes leads to a decrease in the fraction of low redshift contamination as an increasing number of galaxies within $1.4 < z < 2.5$ become visible at fainter K-band limits. Fig. 9 shows clearly how the redshift distribution of BzK galaxies develops a sharper low redshift cut-off as the flux limit is made fainter. By $K_{AB, \text{lim}} \sim 21.5$, the low redshift contamination has fallen to ~ 18 per cent. For fainter flux limits the low redshift contamination decreases much more slowly, reaching ~ 10 per cent by $K_{AB, \text{lim}} \sim 24$.

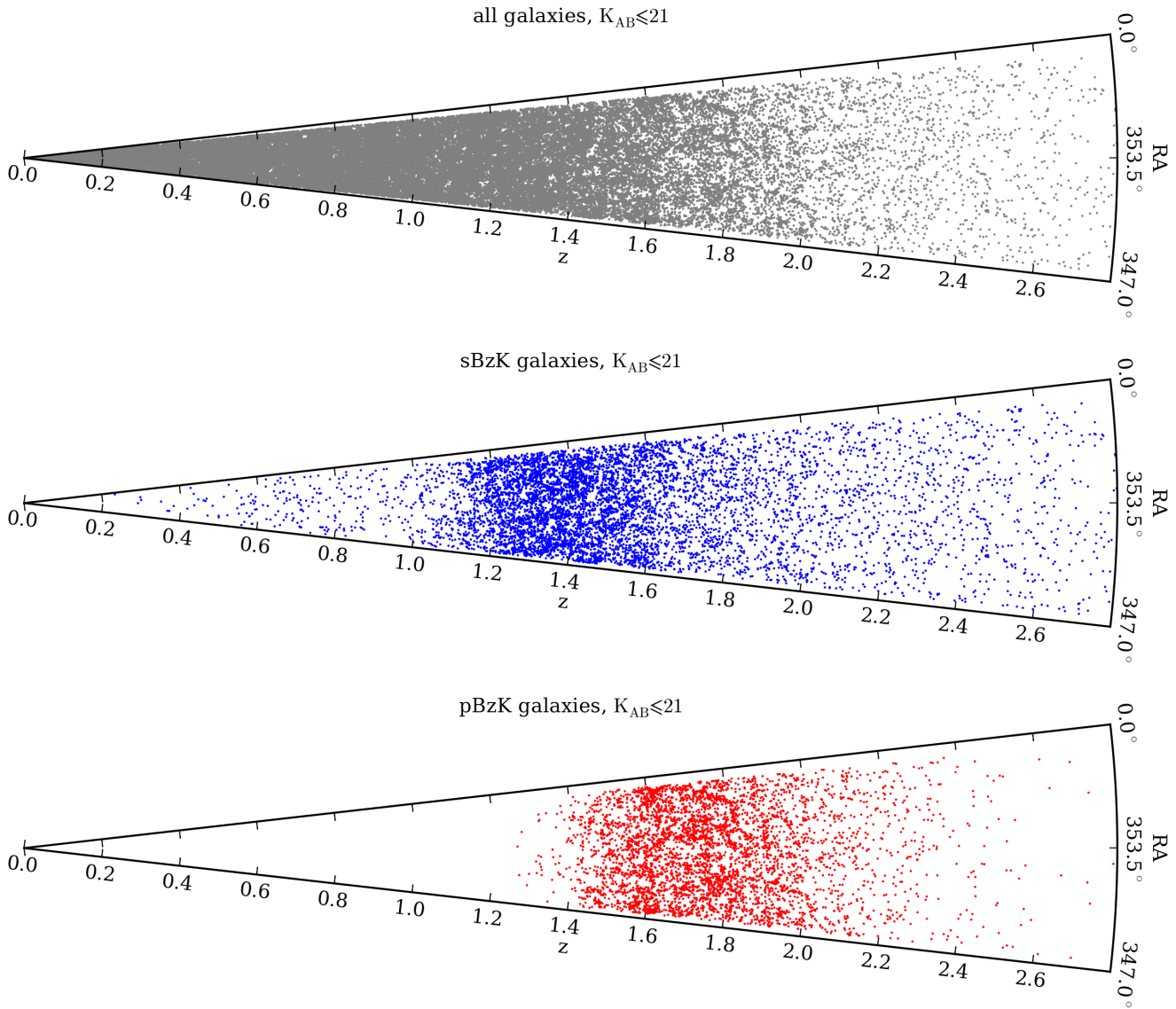


Figure 10. Wedge plots showing a slice in redshift and right ascension, 1° wide in declination, of the predicted distribution of all galaxies with $K_{AB} \leq 21$ (top) and the subsamples of sBzKs (middle) and pBzKs (bottom).

As expected, the fraction of high redshift interlopers increases steadily with increasingly faint limiting K-band magnitude, though it stays well below ~ 20 per cent. By $K_{AB,lim} \sim 23.2$, the contribution from low redshift and high redshift contamination is approximately equal at ~ 12 per cent, with high redshift interlopers dominating the contamination at fainter limiting magnitudes.

Although we have not included the effect of the inter-galactic medium (IGM) attenuation in this particular lightcone, we have checked its effect on the galaxy $(B - z)$ and $(z - K)$ colours. We have examined the $(B - z)$ vs. $(z - K)$ plane at discrete redshift snapshots: $z \sim 2.0$, $z \sim 2.5$ and $z \sim 3$. We find that the IGM attenuation has only a modest affect on the number of BzK galaxies at $z \gtrsim 3$, which is well into the high redshift tail of the galaxy redshift distribution.

5.4.3 Dependence on B-band depth

As we have seen in §5.2, there is evidence that the ability of the BzK technique to distinguish between star-forming and passive galaxies within $1.4 < z < 2.5$ is dependent upon the B-band depth of the galaxy sample. For example, Grazian et al. (2007) determined that 22 per cent of their sample of sBzK galaxies had SEDs typical of passive galaxies rather than star-forming galaxies. A significant number of these galaxies were undetected in the B-band and had their $(B - z)$ colours estimated using a 1σ B-band upper limit, which resulted in their $(B - z)$ colours being too blue. Grazian et al. concluded that, for faint K-band selected galaxies with very red $(z - K)$ colours, a lack of deep B-band photometry will lead to many pBzK galaxies being incorrectly classified as sBzK galaxies.

In Fig. 13, we show the variation of the median B-band apparent magnitude with position in the $(B - z)$ vs. $(z - K)$ plane for $K_{AB} \leq 23$ galaxies in the GALFORM mock catalogue. The trend

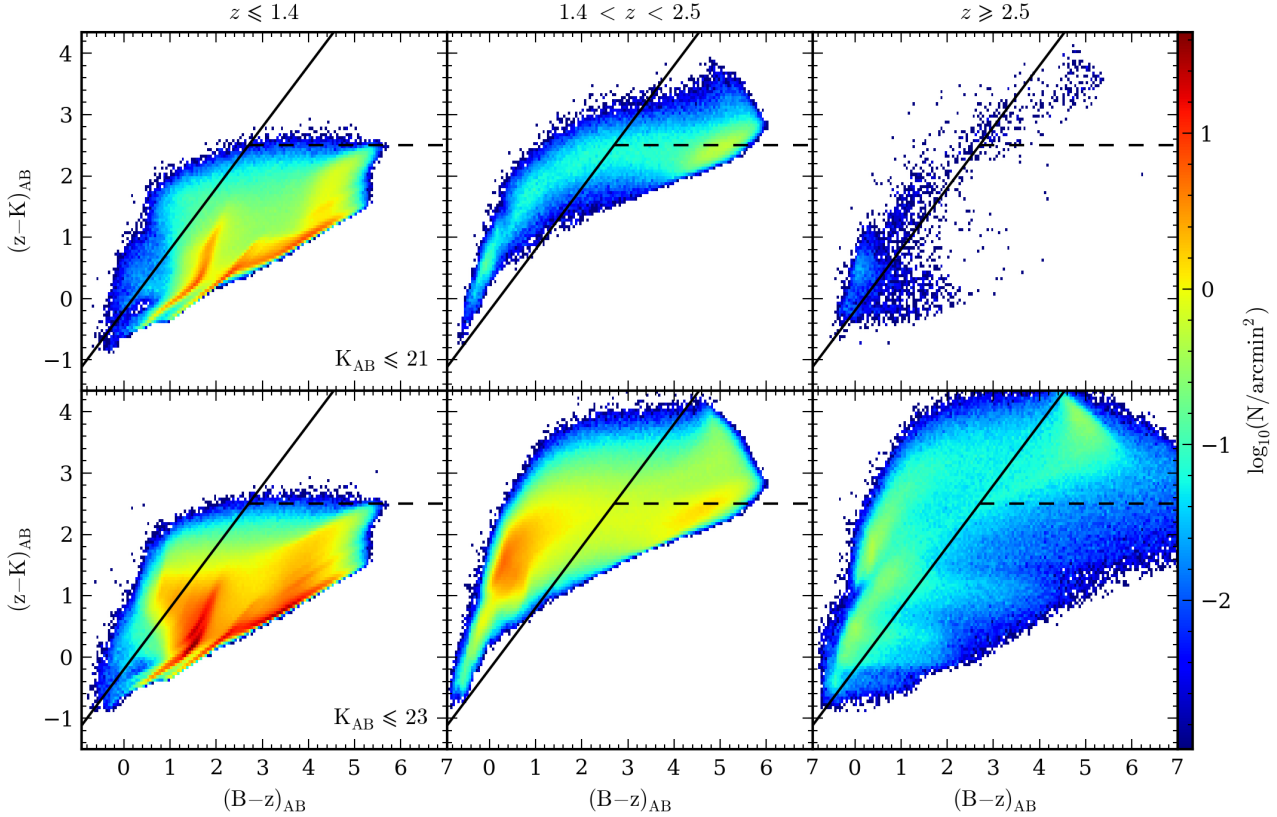


Figure 11. The distribution of synthetic galaxies in the BzK colour plane for two K -band flux limits, $K_{AB} \leq 21$ (top row) and $K_{AB} \leq 23$ (bottom row). The columns correspond to three different redshift ranges: $z \leq 1.4$ (left), $1.4 < z < 2.5$ (the redshift interval which the BzK technique was designed to select, middle) and $z \geq 2.5$ (right). The black solid line and dashed line correspond to the sBzK and pBzK cuts of Daddi et al. (2004a) respectively. The colour shading indicates the surface density of galaxies on the mock sky, as shown by the scale on the right-hand side.

towards fainter B-band magnitudes for redder $(B - z)$ and $(z - K)$ colours is immediately clear and supports the need for deep B-band photometry to probe the faint pBzK population.

We apply a B-band detection limit of $B_{AB,lim} \leq 26$ to a $K_{AB} \leq 23$ sample of galaxies, by assuming that galaxies with B-band magnitudes fainter than $B_{AB,lim}$ are undetected and so have $B_{AB} = B_{AB,lim}$. By doing this, we find that only ~ 0.3 per cent of galaxies within $1.4 < z < 2.5$ are classified as pBzK galaxies. Making the B-band limit fainter leads to a larger fraction of pBzK galaxies. With upper limits of $B_{AB,lim} \leq 27, 28$ and 29 we find that $\sim 3, \sim 9$ and ~ 15 per cent of $1.4 < z < 2.5$ galaxies respectively are classified as pBzK galaxies. An upper limit of $B_{AB,lim} \leq 30$ leads to the same number of pBzK galaxies being recovered (~ 16 per cent) as when applying the $K_{AB} \leq 23$ selection in isolation.

A bright B-band limit will also lead to galaxies that should not be classified as BzK galaxies being scattered into the sBzK region of the $(B - z)$ vs. $(z - K)$ plane. As we have seen in § 5.4.1, for a $K_{AB} \leq 23$ selected galaxy sample, the BzK technique selects ~ 80 per cent of $1.4 < z < 2.5$ galaxies. If we apply B-band detection limits of $B_{AB,lim} \leq 26, 27$ and 28 we find that the BzK technique selects $\sim 95, \sim 87$ and ~ 80 per cent of galaxies within $1.4 < z < 2.5$ respectively.

We conclude that adopting a fainter B-band limit should improve the ability of the BzK technique to distinguish between star-forming and passively evolving galaxies.

5.5 The predicted properties of BzK galaxies

5.5.1 Stellar mass

From the upper left panel of Fig. 5 we can see that the predicted stellar masses of galaxies in a $K_{AB} \leq 23$ selected BzK sample range from $\sim 10^9 h^{-1} M_{\odot}$ to $\sim 10^{11} h^{-1} M_{\odot}$, with the more massive galaxies typically having redder $(z - K)$ colours.

We show in Fig. 14 the distribution of stellar masses for all K-band selected galaxies (within $1.4 < z < 2.5$). The median stellar mass of BzK selected galaxies is in excellent agreement with the distribution for all K-band selected galaxies for all flux limits fainter than $K_{AB,lim} \sim 21$. Additionally, the 10 and 90 percentiles of the BzK distribution consistently match the 10 and 90 percentiles for the stellar mass distribution of the whole galaxy population.

Early studies of BzK galaxies, using K-band limits of $K_{AB} \lesssim 22$, inferred BzK galaxies to be very massive, with typical stellar masses⁸ of $M_{*} \gtrsim 5 \times 10^{10} h^{-1} M_{\odot}$ (Daddi et al. 2004b,a, 2005b,a; Reddy et al. 2005; Kong et al. 2006; Blanc et al. 2008). In Fig. 14 we show the median stellar mass of BzK selected galaxies (within $1.4 < z < 2.5$) as a function of the K-band flux limit. For $K_{AB} \leq 22$, the distribution of BzK stellar masses in the mock catalogue is

⁸ The quoted value for the observed mass has been multiplied by a factor of 1.4 (Fontana et al. 2004) in order to account for the change from Salpeter (1955) IMF, used in observational studies, to the Kennicutt (1983) IMF used for the study presented here.

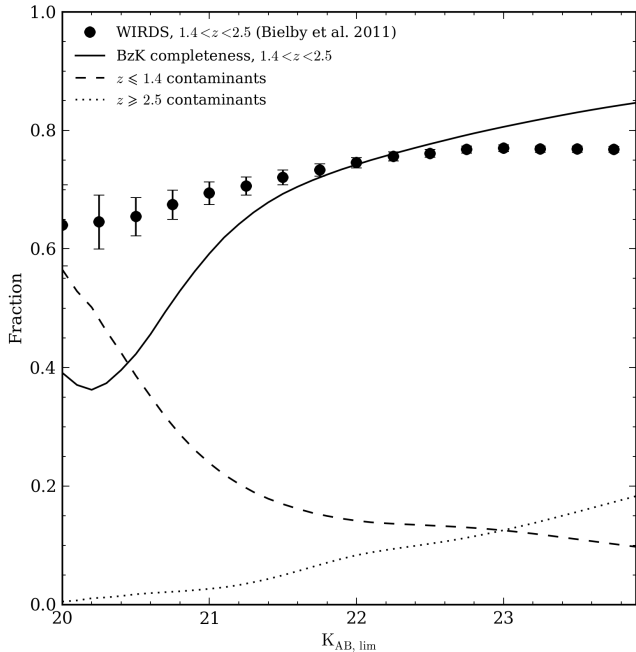


Figure 12. The efficiency of the BzK selection as a function of K -band limiting magnitude, $K_{AB, \text{lim}}$. The solid line shows the predicted fraction of GALFORM galaxies within $1.4 < z < 2.5$, with $K_{AB} \leq K_{AB, \text{lim}}$, that are identified as BzK galaxies. The filled circles correspond to completeness estimates for observed galaxies in the WIRCam Deep Survey (WIRDS, Bielby et al. 2011) that have been calculated in the same way as the GALFORM predictions. The error bars shown correspond to Poisson errors. The dashed and dotted lines show the predicted fraction of interlopers at $z \leq 1.4$ and $z \geq 2.5$ respectively, as a function of K -band limiting magnitude.

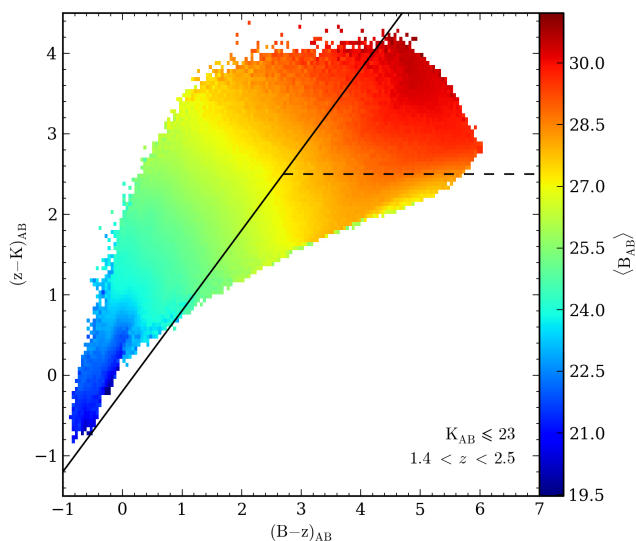


Figure 13. The variation in the median B -band apparent magnitude of galaxies with position in the $(B-z)$ vs. $(z-K)$ plane. The distribution shown corresponds to GALFORM galaxies, within $1.4 < z < 2.5$, selected to have $K_{AB} \leq 23$ and placed into 2-dimensional bins spanning the BzK colour-colour space. The bins are coloured according to the median B -band magnitude of the galaxies in that bin, as shown by the colourbar.

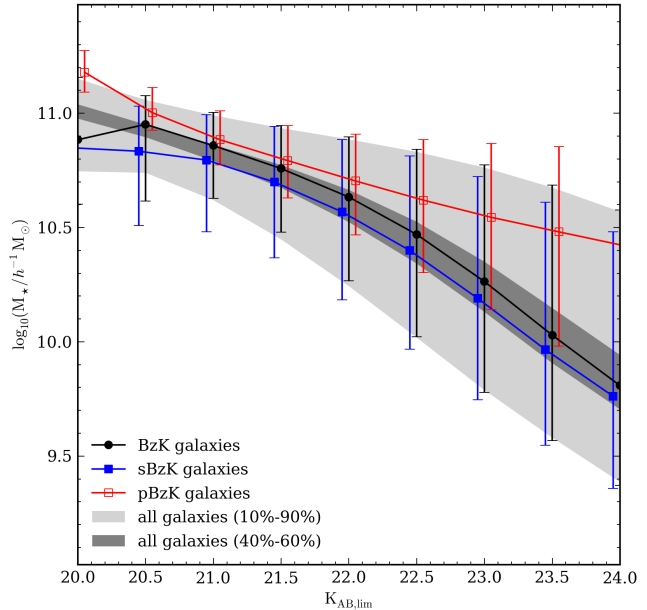


Figure 14. The predicted stellar mass of galaxies with redshift $1.4 < z < 2.5$, as a function of K -band limiting magnitude for all BzK galaxies (black circles), sBzK galaxies (blue, filled squares) and pBzK galaxies (red, open squares). Data points correspond to median values and error bars show the 10 and 90 percentiles. For clarity, the data points for the sBzK and pBzK values have been offset horizontally. The light and dark grey regions show the 10–90 and 40–60 percentiles for all galaxies brighter than the K -band flux limit (i.e. irrespective of whether they are BzK selected).

consistent with observations. Increasing the depth in the K -band, leads to a shift in the distribution towards smaller stellar masses, with a median BzK stellar mass of $\sim 10^{10} h^{-1} M_{\odot}$ being reached at $K_{AB, \text{lim}} \sim 23.5$.

We also show in Fig. 14, the breakdown of the distribution into sBzK and pBzK galaxies. It is immediately clear that, typically, pBzK galaxies are more massive than sBzK galaxies, with the difference between the medians increasing towards fainter K -band limits.

We conclude that BzK selected galaxies appear to provide a representative sample of the galaxy stellar masses at $1.4 < z < 2.5$ and do not appear to be significantly biased towards either very high or low mass galaxies.

5.5.2 Star Formation Rate

As we have already seen in Fig. 5, there is clear trend in the predicted SFR of galaxies across the $(B-z)$ vs. $(z-K)$ plane. In the extremes of the distribution we find that many sBzK selected galaxies are predicted to have SFRs of $\sim 100 h^{-1} M_{\odot} \text{yr}^{-1}$ or more, while many pBzK selected galaxies have SFRs of effectively zero. We find that trend in the specific star-formation rate (SSFR, equal to the star-formation rate of a galaxy divided by its stellar mass) across the $(B-z)$ vs. $(z-K)$ plane is almost identical to that of the star-formation rate.

In Fig. 15 we show the distribution of SFRs for BzK, sBzK and pBzK galaxies, as well as for all K -band selected galaxies, as a function of K -band flux limit, in the redshift range $1.4 < z < 2.5$.

For $K_{AB} \gtrsim 21$, the median SFR for BzK galaxies is in reasonable agreement with the distribution for the whole galaxy pop-

ulation, though is perhaps slightly biased towards higher SFRs. This would, at first, suggest that the BzK selection is missing a fraction of the passive galaxy population, particularly since we have shown in Fig. 8 that the GALFORM mock catalogue matches the number of sBzK galaxies but under-predicts the number of bright pBzK galaxies. It is possible that some fraction of these faint pBzK galaxies are dusty star-forming galaxies that have been mis-classified as being passive. For $K_{AB} \leq 21$, we find that ~ 20 per cent of the pBzK selected galaxies in the GALFORM mock catalogue have SFRs $\gtrsim 0.1 h^{-1} M_{\odot} \text{yr}^{-1}$. Interestingly, the typical SFR of pBzK galaxies remains approximately constant, at $\sim 10^{-4} - 10^{-3} h^{-1} M_{\odot} \text{yr}^{-1}$, with increasing K-band depth (though the distribution is very broad). For $K_{AB, \text{lim}} \gtrsim 23$, the typical SFR of sBzK galaxies also appears to remain almost constant at $\sim 1 - 10 h^{-1} M_{\odot} \text{yr}^{-1}$.

In Fig. 15, we see that the model predicted median SFR of BzK galaxies with $K_{AB} \leq 22$ to be $\sim 1 h^{-1} M_{\odot} \text{yr}^{-1}$. However, observational studies of BzK galaxies with $K_{AB} \lesssim 22$ concluded many of these bright BzK galaxies to be starbursting galaxies, with SFRs of $\sim 50 h^{-2} M_{\odot} \text{yr}^{-1} - 100 h^{-2} M_{\odot} \text{yr}^{-1}$ (e.g. Daddi et al. 2004a; Kong et al. 2006; Blanc et al. 2008). A possible explanation for this discrepancy is the overly efficient shut down of gas cooling by AGN feedback in the Bower et al. (2006) model, which has been previously suggested by Gonzalez-Perez et al. (2009).

Based upon the model predictions however, we predict that, towards fainter K-band limiting magnitudes, the BzK technique is typically selecting galaxies with SFRs that are consistent with the median SFRs of the galaxy population within $1.4 < z < 2.5$.

We note that a trend similar to that seen in the predicted median SFR is seen in the median values of the sSFR of BzK selected galaxies. At faint K-band limits, the median sSFR of BzK and sBzK galaxies tends towards $\sim 10^{-10} \text{yr}^{-1}$. The GALFORM model predicts this value to be typical for K-band selected galaxies at $1.4 < z < 2.5$. As with the median SFR, the median sSFR tends towards a constant value of $\sim 10^{-14} \text{yr}^{-1}$.

5.5.3 Metallicity

We have already seen in § 5.1 that the metallicity of K-band selected galaxies varies with position in the $(B - z)$ vs. $(z - K)$ plane. From the lower left-hand panel of Fig. 5 we can see that galaxies with the reddest $(z - K)$ colours (typically pBzK and faint sBzK galaxies) are in general the most metal rich.

In Fig. 16 we show the metallicity distribution for BzK selected galaxies within $1.4 < z < 2.5$. For all K-band limits considered the metallicity distribution of BzK selected galaxies is in good agreement with the metallicity distribution for all K-band selected galaxies. The trend in the metallicity distribution as a function of K-band flux limit is very similar to the trend seen in the stellar mass distribution in Fig. 14. For brighter K-band flux limits, one would predict to recover BzK galaxies with higher metallicities. For the brightest flux limit considered, the median metallicities for BzK galaxies falls below that for all galaxies. As with the stellar mass distribution, this is due to GALFORM under-predicting the counts of bright pBzK galaxies, which one would expect to be metal-rich. The distributions for the separate sBzK and pBzK subsets show that for any K-band depth, pBzK galaxies will typically be more metal-rich than sBzK galaxies, though the distributions for the two subsets do overlap.

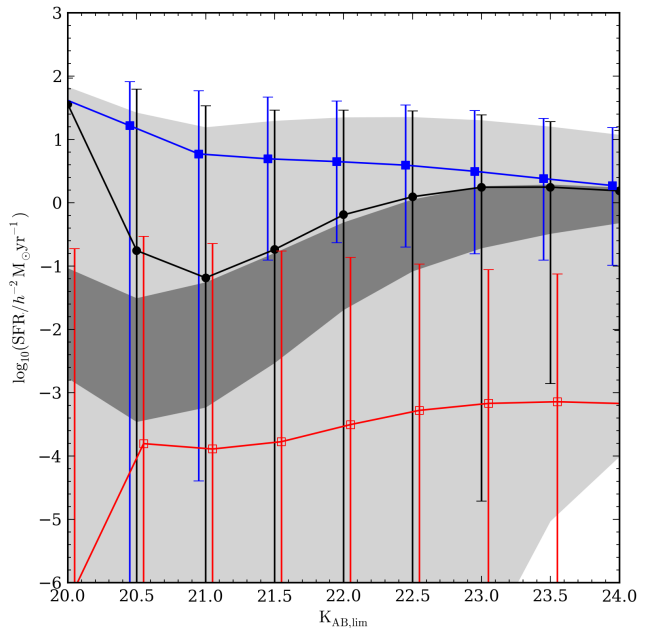


Figure 15. The predicted star-formation rate as a function of K-band limiting magnitude for galaxies in $1.4 < z < 2.5$. The symbols and shaded regions are the same as in Fig. 14.

5.5.4 Age

In the lower right-hand panel of Fig. 5 we show the median stellar mass weighted age of galaxies in the $(B - z)$ vs. $(z - K)$ plane. We find that the oldest galaxies occupy the region where the density of passive galaxies peaks just below the pBzK region, as can be seen in the middle column of Fig. 11. The vast majority of the oldest galaxies, with ages above 2 Gyr, that fall outside the pBzK region lie within the redshift interval $1.4 < z < 2.5$. This is due to the finite width of the 4000\AA break, which at $z \sim 1.4$ is beginning to enter the response curve of the z-band, thus making the $(z - K)$ colours of these galaxies bluer. Above $z = 2$, all of the galaxies with ages above approximately 1.5 Gyr lie well within the pBzK region on the colour plane. We have checked that the $(z - K)$ colours of the galaxies are not significantly affected by changing between a Kennicutt (1983) and a Salpeter (1955) IMF.

We show in Fig. 17 the distribution of the stellar mass weighted ages for all K-band selected galaxies and for those that are BzK-selected. Like the distribution of SFRs, the distribution of ages of BzK galaxies is in reasonable agreement with the age distribution for all K-band selected galaxies, though appears to be slightly biased towards younger galaxies. As with the SFR distribution, we see that the typical ages of sBzK and pBzK galaxies remain approximately constant (at ~ 1.1 Gyr and ~ 1.7 Gyr respectively) for $K_{AB, \text{lim}} \gtrsim 22$.

5.5.5 Dust

Reddening due to dust can mimic a large break at 4000\AA in the spectra of star-forming $z \lesssim 1.4$ galaxies (Kriek et al. 2006, 2011). However, many authors have argued that the effectiveness of the BzK colour selection is not significantly affected by dust extinction (e.g. Daddi et al. 2004a; Kong et al. 2006; Hayashi et al. 2007;

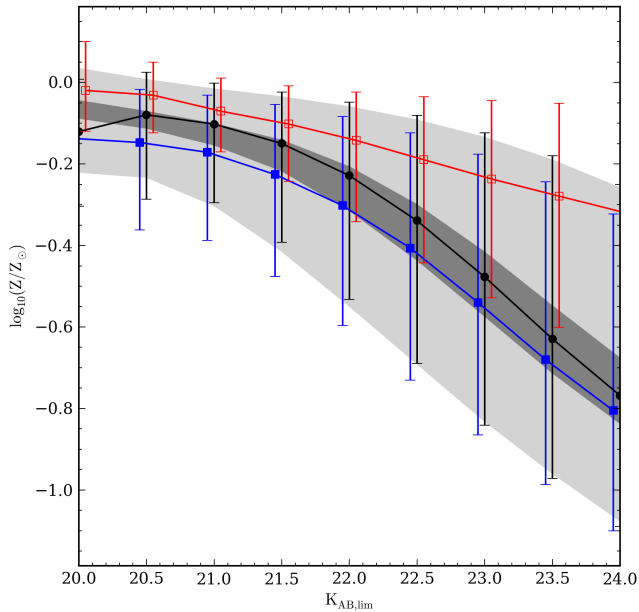


Figure 16. The predicted stellar metallicity as a function of K-band limiting magnitude for galaxies in $1.4 < z < 2.5$. The symbols and shaded regions are the same as in Fig. 14.

Grazian et al. 2007; Hartley et al. 2008; Hayashi et al. 2009; Lin et al. 2011).

For the K-band limits considered in Fig. 11 we find that in the presence of dust the distribution of $1.4 < z < 2.5$ galaxies in the $(B - z)$ vs. $(z - K)$ plane remains relatively unchanged, aside from an increased scatter in the sBzK galaxy population towards redder $(z - K)$ colours. We find that for $K_{AB} \leq 23$ the presence of dust reddens the colours of BzK galaxies, within $1.4 < z < 2.5$, by $\Delta(B - z) \sim 0.15$ and $\Delta(z - K) \sim 0.3$. The presence of dust appears to have a greater effect on the median colours of sBzK galaxies, as we find a negligible change in the median colours of pBzK galaxies. We can see this also in Fig. 8 where the number counts of sBzK galaxies without dust extinction are boosted by ~ 1 dex, while the pBzK number counts remain the same. The reduction in the sBzK counts when dust extinction is included is likely due to dust reddening the $(B - z)$ colours of star-forming galaxies (with $(z - K)_{AB} < 2.5$) and scattering them out of the sBzK region.

6 CONCLUSIONS

We have presented a method for constructing end-to-end mock galaxy catalogues by applying a semi-analytical model of galaxy formation to the halo merger trees extracted from a cosmological N-body simulation. The mocks that we construct are *lightcone* catalogues, in which a galaxy is placed according to the epoch at which it first enters the past lightcone of the observer. Thus our catalogues incorporate the evolution of galaxy properties that is predicted over the simulation snapshots. We use interpolation to determine the positions of galaxies at epochs intermediate to the simulation snapshots, which represents an improvement over previous work. We have shown that our adopted interpolation scheme leads to accurate predictions for real space galaxy clustering down to scales well within the one-halo regime.

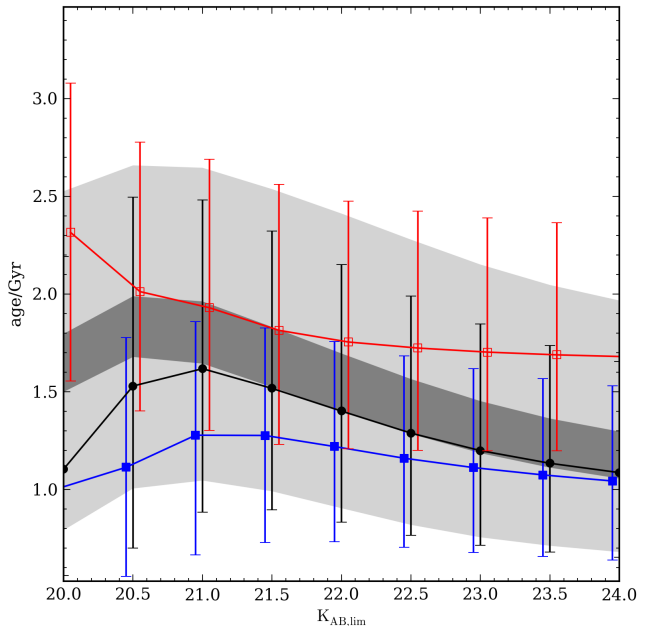


Figure 17. The predicted stellar mass weighted age as a function of K-band limiting magnitude for galaxies in $1.4 < z < 2.5$. The symbols and shaded regions are the same as in Fig. 14.

We can summarise our method for constructing lightcone catalogues as follows:

- (i) Populate the dark matter halos in the snapshot outputs of a cosmological N-body simulation with galaxies using a physical model of galaxy formation, giving populations of galaxies at a range of cosmic epochs. Here we use the dark matter halos from the *Millennium Simulation* (Springel et al. 2005), which we populate with galaxies, whose positions and properties are calculated using the GALFORM semi-analytical model. (In this work we adopt the Bower et al. (2006) version of GALFORM.)
- (ii) Position an observer within the simulation box. Replicate the simulation box to span a cosmological volume that is of sufficient size to encompass the galaxy survey that we wish to mimic.
- (iii) For replication of the box, use adjacent pairs of simulation snapshots to determine the epoch at which each galaxy enters the observer's past lightcone. Use interpolation to determine the corresponding position of the galaxy at this epoch. Reject all galaxies that enter the observer's lightcone at a position outside of the solid-angle of the galaxy survey.
- (iv) Assign each galaxy that enters the lightcone the intrinsic properties that the galaxy had at the lowest redshift snapshot prior to the galaxy entering the lightcone. Use the position of the galaxy to convert luminosities and absolute magnitudes into observed fluxes and apparent magnitudes. Reject all galaxies that fall outside of the flux limits which define the galaxy survey.

Our approach has a number of attractive features. First, we use a physical model of galaxy formation which makes *ab initio* predictions. This means that we can build mocks for epochs or selections which are currently unprobed. Empirical approaches are not able to do this, as they depend on the existence of observations. Second, our construction method is generic and is not tied to a particular choice of N-body simulation or semi-analytic model. As better N-body simulations or more accurate galaxy formation models

become available, our method can still be used. Third, the semi-analytic model that we have used has a unique multi-wavelength capability, which means that we can mimic surveys built using many different telescopes such as GAMA.

As an illustrative application of our method we considered the effectiveness of the BzK colour selection technique which is designed to isolate galaxies within the redshift range $1.4 < z < 2.5$ (Daddi et al. 2004a). The aim of this exercise is to determine how successful this technique is at isolating galaxies within the target redshift range and whether the galaxies it selects are representative of the target population or a biased subsample.

The GALFORM model is able to match reasonably well the K-band number counts of all BzK galaxies, as well as the counts of sBzK galaxies. However, the model under-predicts the number of bright pBzK galaxies and over-predicts the number of faint pBzK galaxies. The latter discrepancy is partially due to the effect of the depth of B-band photometry, but may also be related to the crude estimate of the stripping of gas from satellite galaxies that is carried out in the Bower et al. (2006) model. The BzK technique successfully selects the majority of the galaxy population within $2 \lesssim z < 2.5$ (and possibly out as far as $z \sim 3$), though is less efficient for $1.4 < z \lesssim 2.0$. Examination of the effectiveness of the BzK technique as a function of K-band limiting magnitude suggests that the technique recovers $\gtrsim 75$ per cent of the $1.4 < z < 2.5$ galaxy population for K-band limits fainter than $K_{AB} \sim 22$. For brighter limits the completeness decreases substantially as the BzK population becomes dominated by low redshift interlopers with $z \leq 1.4$. For magnitude limits $K_{AB} \gtrsim 21.5$, the fraction of contamination from BzK galaxies outside $1.4 < z < 2.5$, remains approximately constant at ~ 30 per cent. We have also shown that a variation in the typical B-band magnitude across the BzK plane can lead to the mis-classification of pBzK galaxies as sBzK galaxies if the B-band photometry is of insufficient depth. Finally, we considered the intrinsic properties of BzK galaxies, including their stellar mass, SFR, metallicity and stellar mass weighted age. We find that BzK galaxies display distributions of these various properties that are in good agreement with the corresponding distributions for all galaxies with $K_{AB} \gtrsim 20.5$. However, at brighter K-band limits BzK galaxies appear to be less massive, more star-forming, less metal-rich and younger than the overall population. This is likely related to the under-prediction of the bright pBzK number counts. The presence of dust increases the scatter in the colours of (faint) sBzK galaxies, though does not dramatically change the colour distribution of galaxies within $1.4 < z < 2.5$.

We conclude that the BzK colour selection does provide a representative sample of the $1.4 < z < 2.5$ population, working better for fainter K-band flux limits. However, the depth of B-band photometry and extinction due to dust may lead to confusion between the sBzK and pBzK subsets.

The tool that we have developed in this paper is a valuable resource to aid in the exploitation of a wide range of surveys, from traditional optical selection to novel properties, such as the neutral hydrogen content of galaxies. Lightcone mock catalogues for different surveys will be made available for download at <http://www.dur.ac.uk/a.i.merson/lightcones.html>.

ACKNOWLEDGMENTS

We thank David Murphy and Daniel Farrow for many useful discussions and suggestions and Emanuele Daddi for provision of the

B, z and K filter response curves. AIM acknowledges the support of a Science and Technologies Facilities Council (STFC) studentship. PN acknowledges a Royal Society URF and an ERC StG grant (DEGAS-259586). Calculations for this paper were performed on the ICC Cosmology Machine, which is part of the DiRAC Facility jointly funded by STFC, the Large Facilities Capital Fund of BIS and Durham University. This work was supported by a rolling grant from the STFC.

REFERENCES

- Almeida C., Baugh C. M., Wake D. A., Lacey C. G., Benson A. J., Bower R. G., Pimblet K., 2008, *MNRAS*, 386, 2145
- Alpaslan M., Robotham A. S. G., Driver S., Norberg P., Peacock J. A., Baldry I., Bland-Hawthorn J., Brough S. et al, 2012, *MNRAS*, 3012
- Arnouts S., Vandame B., Benoist C., Groenewegen M. A. T., da Costa L., Schirmer M., Mignani R. P., Slijkhuis R. et al, 2001, *A&A*, 379, 740
- Baugh C. M., 2006, *Reports on Progress in Physics*, 69, 3101
- , 2008, *Royal Society of London Philosophical Transactions Series A*, 366, 4381
- Baugh C. M., Lacey C. G., Frenk C. S., Granato G. L., Silva L., Bressan A., Benson A. J., Cole S., 2005, *MNRAS*, 356, 1191
- Benson A. J., 2010, *Phys. Rep.*, 495, 33
- Benson A. J., Baugh C. M., Cole S., Frenk C. S., Lacey C. G., 2000, *MNRAS*, 316, 107
- Benson A. J., Bower R., 2010, *MNRAS*, 405, 1573
- Benson A. J., Bower R. G., Frenk C. S., Lacey C. G., Baugh C. M., Cole S., 2003, *ApJ*, 599, 38
- Berlind A. A., Weinberg D. H., 2002, *ApJ*, 575, 587
- Bielby R., Hudelot P., McCracken H. J., Ilbert O., Daddi E., Le Fèvre O., Gonzalez-Perez V., Kneib J.-P. et al, 2011, *arXiv:astro-ph/1111.6997*
- Blaizot J., Wadadekar Y., Guiderdoni B., Colombi S. T., Bertin E., Bouchet F. R., Devriendt J. E. G., Hatton S., 2005, *MNRAS*, 360, 159
- Blanc G. A., Lira P., Barrientos L. F., Aguirre P., Francke H., Taylor E. N., Quadri R., Marchesini D. et al, 2008, *ApJ*, 681, 1099
- Blanton M. R., Roweis S., 2007, *AJ*, 133, 734
- Bower R. G., Benson A. J., Malbon R., Helly J. C., Frenk C. S., Baugh C. M., Cole S., Lacey C. G., 2006, *MNRAS*, 370, 645
- Bower R. G., Vernon I., Goldstein M., Benson A. J., Lacey C. G., Baugh C. M., Cole S., Frenk C. S., 2010, *MNRAS*, 407, 2017
- Bruzual G., Charlot S., 2003, *MNRAS*, 344, 1000
- Cai Y.-C., Angulo R. E., Baugh C. M., Cole S., Frenk C. S., Jenkins A., 2009, *MNRAS*, 395, 1185
- Capak P., Cowie L. L., Hu E. M., Barger A. J., Dickinson M., Fernandez E., Giavalisco M., Komiyama Y. et al, 2004, *AJ*, 127, 180
- Carlson J., White M., 2010, *ApJS*, 190, 311
- Cole S., 1991, *ApJ*, 367, 45
- Cole S., Aragon-Salamanca A., Frenk C. S., Navarro J. F., Zepf S. E., 1994, *MNRAS*, 271, 781
- Cole S., Hatton S., Weinberg D. H., Frenk C. S., 1998, *MNRAS*, 300, 945
- Cole S., Lacey C. G., Baugh C. M., Frenk C. S., 2000, *MNRAS*, 319, 168
- Cole S., Percival W. J., Peacock J. A., Norberg P., Baugh C. M., Frenk C. S., Baldry I., Bland-Hawthorn J. et al, 2005, *MNRAS*, 362, 505

- Colless M., Dalton G., Maddox S., Sutherland W., Norberg P., Cole S., Bland-Hawthorn J., Bridges T. et al, 2001, *MNRAS*, 328, 1039
- Colless M., Peterson B. A., Jackson C., Peacock J. A., Cole S., Norberg P., Baldry I. K., Baugh C. M. et al, 2003, arXiv:astro-ph/0306581
- Daddi E., Cimatti A., Renzini A., Fontana A., Mignoli M., Pozzetti L., Tozzi P., Zamorani G., 2004a, *ApJ*, 617, 746
- Daddi E., Cimatti A., Renzini A., Vernet J., Conselice C., Pozzetti L., Mignoli M., Tozzi P. et al, 2004b, *ApJ*, 600, L127
- Daddi E., Dickinson M., Chary R., Pope A., Morrison G., Alexander D. M., Bauer F. E., Brandt W. N. et al, 2005a, *ApJ*, 631, L13
- Daddi E., Renzini A., Pirzkal N., Cimatti A., Malhotra S., Stiavelli M., Xu C., Pasquali A. et al, 2005b, *ApJ*, 626, 680
- Davis M., Efstathiou G., Frenk C. S., White S. D. M., 1985, *ApJ*, 292, 371
- Diaferio A., Kauffmann G., Colberg J. M., White S. D. M., 1999, *MNRAS*, 307, 537
- Dickinson M., Papovich C., Ferguson H. C., Budavári T., 2003, *ApJ*, 587, 25
- Driver S. P., Hill D. T., Kelvin L. S., Robotham A. S. G., Liske J., Norberg P., Baldry I. K., Bamford S. P. et al, 2011, *MNRAS*, 413, 971
- Driver S. P., Norberg P., Baldry I. K., Bamford S. P., Hopkins A. M., Liske J., Loveday J., Peacock J. A. et al, 2009, *Astronomy and Geophysics*, 50, 050000
- Eke V. R., Baugh C. M., Cole S., Frenk C. S., Norberg P., Peacock J. A., Baldry I. K., Bland-Hawthorn J. et al, 2004, *MNRAS*, 348, 866
- Elston R., Rieke G. H., Rieke M. J., 1988, *ApJ*, 331, L77
- Fanidakis N., Baugh C. M., Benson A. J., Bower R. G., Cole S., Done C., Frenk C. S., 2011, *MNRAS*, 410, 53
- Ferguson H. C., Dickinson M., Williams R., 2000, *ARA&A*, 38, 667
- Fioc M., Rocca-Volmerange B., 1999, arXiv:astro-ph/9912179
- Font A. S., Bower R. G., McCarthy I. G., Benson A. J., Frenk C. S., Helly J. C., Lacey C. G., Baugh C. M. et al, 2008, *MNRAS*, 389, 1619
- Fontana A., Pozzetti L., Donnarumma I., Renzini A., Cimatti A., Zamorani G., Menci N., Daddi E. et al, 2004, *A&A*, 424, 23
- Franx M., Labbé I., Rudnick G., van Dokkum P. G., Daddi E., Förster Schreiber N. M., Moorwood A., Rix H.-W. et al, 2003, *ApJ*, 587, L79
- Gao L., Springel V., White S. D. M., 2005, *MNRAS*, 363, L66
- González J. E., Lacey C. G., Baugh C. M., Frenk C. S., Benson A. J., 2009, *MNRAS*, 397, 1254
- Gonzalez-Perez V., Baugh C. M., Lacey C. G., Almeida C., 2009, *MNRAS*, 398, 497
- Granato G. L., Lacey C. G., Silva L., Bressan A., Baugh C. M., Cole S., Frenk C. S., 2000, *ApJ*, 542, 710
- Grazian A., Salimbeni S., Pentericci L., Fontana A., Nonino M., Vanzella E., Cristiani S., de Santis C. et al, 2007, *A&A*, 465, 393
- Hartley W. G., Lane K. P., Almaini O., Cirasuolo M., Foucaud S., Simpson C., Maddox S., Smail I. et al, 2008, *MNRAS*, 391, 1301
- Hayashi M., Motohara K., Shimasaku K., Onodera M., Uchimoto Y. K., Kashikawa N., Yoshida M., Okamura S. et al, 2009, *ApJ*, 691, 140
- Hayashi M., Shimasaku K., Motohara K., Yoshida M., Okamura S., Kashikawa N., 2007, *ApJ*, 660, 72
- Henriques B. M. B., White S. D. M., Lemson G., Thomas P. A., Guo Q., Marleau G.-D., Overzier R. A., 2012, *MNRAS*, 421, 2904
- Ilbert O., Salvato M., Le Flocc'h E., Aussel H., Capak P., McCracken H. J., Mobasher B., Kartaltepe J. et al, 2010, *ApJ*, 709, 644
- Imai K., Pearson C. P., Matsuhara H., Wada T., Oyabu S., Takagi T., Fujishiro N., Hanami H., 2008, *ApJ*, 683, 45
- Iovino A., McCracken H. J., Garilli B., Foucaud S., Le Fèvre O., Maccagni D., Saracco P., Bardelli S. et al, 2005, *A&A*, 442, 423
- Kashikawa N., Shimasaku K., Yasuda N., Ajiki M., Akiyama M., Ando H., Aoki K., Doi M. et al, 2004, *PASJ*, 56, 1011
- Kauffmann G., Heckman T. M., White S. D. M., Charlot S., Tremonti C., Brinchmann J., Bruzual G., Peng E. W. et al, 2003, *MNRAS*, 341, 33
- Kauffmann G., White S. D. M., Guiderdoni B., 1993, *MNRAS*, 264, 201
- Keenan R. C., Trouille L., Barger A. J., Cowie L. L., Wang W.-H., 2010, *ApJS*, 186, 94
- Kennicutt Jr. R. C., 1983, *ApJ*, 272, 54
- Kitzbichler M. G., White S. D. M., 2007, *MNRAS*, 376, 2
- Kong X., Daddi E., Arimoto N., Renzini A., Broadhurst T., Cimatti A., Ikuta C., Ohta K. et al, 2006, *ApJ*, 638, 72
- Kriek M., van Dokkum P. G., Franx M., Förster Schreiber N. M., Gawiser E., Illingworth G. D., Labbé I., Marchesini D. et al, 2006, *ApJ*, 645, 44
- Kriek M., van Dokkum P. G., Whitaker K. E., Labbé I., Franx M., Brammer G. B., 2011, *ApJ*, 743, 168
- Lacey C. G., Baugh C. M., Frenk C. S., Benson A. J., Orsi A., Silva L., Granato G. L., Bressan A., 2010, *MNRAS*, 405, 2
- Lacey C. G., Baugh C. M., Frenk C. S., Silva L., Granato G. L., Bressan A., 2008, *MNRAS*, 385, 1155
- Lagos C. D. P., Baugh C. M., Lacey C. G., Benson A. J., Kim H.-S., Power C., 2011a, *MNRAS*, 418, 1649
- Lagos C. d. P., Bayet E., Baugh C. M., Lacey C. G., Bell T., Fanidakis N., Geach J., 2012, arXiv:astro-ph/1204.0795
- Lagos C. D. P., Lacey C. G., Baugh C. M., Bower R. G., Benson A. J., 2011b, *MNRAS*, 416, 1566
- Lane K. P., Almaini O., Foucaud S., Simpson C., Smail I., McLure R. J., Conselice C. J., Cirasuolo M. et al, 2007, *MNRAS*, 379, L25
- Lilly S. J., Cowie L. L., Gardner J. P., 1991, *ApJ*, 369, 79
- Lin L., Dickinson M., Jian H.-Y., Merson A. I., Baugh C. M., Scott D., Foucaud S., Wang W.-H. et al, 2011, arXiv:astro-ph/1111.2135
- Madau P., Pozzetti L., Dickinson M., 1998, *ApJ*, 498, 106
- McBride C., Berlind A., Scoccimarro R., Wechsler R., Busha M., Gardner J., van den Bosch F., 2009, in *Bulletin of the American Astronomical Society*, Vol. 41, American Astronomical Society Meeting Abstracts 213, p. 425.06
- McCarthy P. J., 2004, *ARA&A*, 42, 477
- McCracken H. J., Capak P., Salvato M., Aussel H., Thompson D., Daddi E., Sanders D. B., Kneib J.-P. et al, 2010, *ApJ*, 708, 202
- McCracken H. J., Radovich M., Bertin E., Mellier Y., Dantel-Fort M., Le Fèvre O., Cuillandre J. C., Gwyn S. et al, 2003, *A&A*, 410, 17
- Metcalfe N., Shanks T., Weilbacher P. M., McCracken H. J., Fong R., Thompson D., 2006, *MNRAS*, 370, 1257
- Murphy D. N. A., Geach J. E., Bower R. G., 2012, *MNRAS*, 420, 1861
- Norberg P., Baugh C. M., Hawkins E., Maddox S., Madgwick D., Lahav O., Cole S., Frenk C. S. et al, 2002, *MNRAS*, 332, 827
- Norberg P., Baugh C. M., Hawkins E., Maddox S., Peacock J. A., Cole S., Frenk C. S., Bland-Hawthorn J. et al, 2001, *MNRAS*,

- 328, 64
- Oke J. B., Gunn J. E., 1983, *ApJ*, 266, 713
- Orsi A., Baugh C. M., Lacey C. G., Cimatti A., Wang Y., Zamorani G., 2010, *MNRAS*, 405, 1006
- Overzier R., Lemson G., Angulo R. E., Bertin E., Blaizot J., Henriques B. M. B., Marleau G.-D., White S. D. M., 2012, [arXiv:astro-ph/1206.6923](https://arxiv.org/abs/1206.6923)
- Overzier R. A., Guo Q., Kauffmann G., De Lucia G., Bouwens R., Lemson G., 2009, *MNRAS*, 394, 577
- Quadri R., Marchesini D., van Dokkum P., Gawiser E., Franx M., Lira P., Rudnick G., Urry C. M. et al, 2007, *AJ*, 134, 1103
- Reddy N. A., Erb D. K., Steidel C. C., Shapley A. E., Adelberger K. L., Pettini M., 2005, *ApJ*, 633, 748
- Robotham A. S. G., Norberg P., Driver S. P., Baldry I. K., Bamford S. P., Hopkins A. M., Liske J., Loveday J. et al, 2011, *MNRAS*, 416, 2640
- Rovilos E., Burwitz V., Szokoly G., Hasinger G., Egami E., Bouché N., Berta S., Salvato M. et al, 2009, *A&A*, 507, 195
- Salpeter E. E., 1955, *ApJ*, 121, 161
- Sánchez A. G., Baugh C. M., Percival W. J., Peacock J. A., Padilla N. D., Cole S., Frenk C. S., Norberg P., 2006, *MNRAS*, 366, 189
- Sánchez A. G., Crocce M., Cabré A., Baugh C. M., Gaztañaga E., 2009, *MNRAS*, 400, 1643
- Sanchez A. G., Scoccola C. G., Ross A. J., Percival W., Manera M., Montesano F., Mazzalay X., Cuesta A. J. et al, 2012, [arXiv:astro-ph/1203.6616](https://arxiv.org/abs/1203.6616)
- Saracco P., Giallongo E., Cristiani S., D'Odorico S., Fontana A., Iovino A., Poli F., Vanzella E., 2001, *A&A*, 375, 1
- Schaye J., Dalla Vecchia C., Booth C. M., Wiersma R. P. C., Theuns T., Haas M. R., Bertone S., Duffy A. R. et al, 2010, *MNRAS*, 402, 1536
- Song J., Mohr J. J., Barkhouse W. A., Warren M. S., Dolag K., Rude C., 2012, *ApJ*, 747, 58
- Sousbie T., Courtois H., Bryan G., Devriendt J., 2008, *ApJ*, 678, 569
- Spergel D. N., Verde L., Peiris H. V., Komatsu E., Nolte M. R., Bennett C. L., Halpern M., Hinshaw G. et al, 2003, *ApJS*, 148, 175
- Springel V., 2005, *MNRAS*, 364, 1105
- Springel V., White S. D. M., Jenkins A., Frenk C. S., Yoshida N., Gao L., Navarro J., Thacker R. et al, 2005, *Nature*, 435, 629
- Springel V., White S. D. M., Tormen G., Kauffmann G., 2001, *MNRAS*, 328, 726
- Steidel C. C., Adelberger K. L., Shapley A. E., Pettini M., Dickinson M., Giavalisco M., 2003, *ApJ*, 592, 728
- Steidel C. C., Giavalisco M., Pettini M., Dickinson M., Adelberger K. L., 1996, *ApJ*, 462, L17
- Steidel C. C., Shapley A. E., Pettini M., Adelberger K. L., Erb D. K., Reddy N. A., Hunt M. P., 2004, *ApJ*, 604, 534
- Tegmark M., Eisenstein D. J., Strauss M. A., Weinberg D. H., Blanton M. R., Frieman J. A., Fukugita M., Gunn J. E. et al, 2006, *Phys. Rev. D*, 74, 123507
- Vale A., Ostriker J. P., 2004, *MNRAS*, 353, 189
- van Dokkum P. G., Förster Schreiber N. M., Franx M., Daddi E., Illingworth G. D., Labbé I., Moorwood A., Rix H.-W. et al, 2003, *ApJ*, 587, L83
- Vandame B., Olsen L. F., Jorgensen H. E., Groenewegen M. A. T., Schirmer M., Arnouts S., Benoist C., da Costa L. et al, 2001, [arXiv:astro-ph/0102300](https://arxiv.org/abs/astro-ph/0102300)
- White S. D. M., Frenk C. S., 1991, *ApJ*, 379, 52
- White S. D. M., Rees M. J., 1978, *MNRAS*, 183, 341
- York D. G., Adelman J., Anderson Jr. J. E., Anderson S. F., Annis J., Bahcall N. A., Bakken J. A., Barkhouser R. et al, 2000, *AJ*, 120, 1579
- Zehavi I., Zheng Z., Weinberg D. H., Blanton M. R., Bahcall N. A., Berlind A. A., Brinkmann J., Frieman J. A. et al, 2011, *ApJ*, 736, 59
- Zehavi I., Zheng Z., Weinberg D. H., Frieman J. A., Berlind A. A., Blanton M. R., Scoccamarro R., Sheth R. K. et al, 2005, *ApJ*, 630, 1